

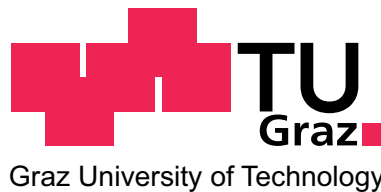
Alexander Meierhofer

**Simulation of ammonia sensitive organic
field-effect transistors by a two-dimensional
drift-diffusion model**

MASTER THESIS

For obtaining the academic degree
Diplom-Ingenieur

Diploma Programme of
Technical Physics



Graz University of Technology

Supervisor:

Ao. Univ.-Prof. Dr. Ferdinand Schürer

Co-Supervisor:

Dipl.-Phys. Dr.rer.nat. Karin Zojer

Institute of Theoretical and Computational Physics

Graz, September 2010

Abstract

Organic thin-film field-effect transistors (OTFTs) can act as ammonia sensors if, e.g., an NH_3 sensitive polymer is incorporated as isolating material. It has been experimentally demonstrated that a particular setup containing an Eosin-Y functionalized ROM-polymer responds to NH_3 exposure by 800% increase in current. To elucidate the underlying sensing mechanism, the carrier transport is simulated by using a two-dimensional drift-diffusion model in this thesis. The corresponding system of equations, containing the Poisson equation, current density equations and the continuity equation, is solved self-consistently on a two-dimensional non-regular grid. The influence of important parameters, i.e., the height of the injection barrier, the mobility, different dielectric constants, and the substrate potential, is studied. By using a set of parameters justified by the aforementioned study, the I-V curves of the device without the presence of ammonia are obtained. Further calculations incorporating potential sensing scenarios demonstrated that the ammonia induced changes in the OTFT operation originate from a surface layer of negative charges formed by deprotonated hydroxyl groups located at the organic semiconductor-isolator interface.

Simulation von Ammoniak sensitiven Feldeffekttransistoren mit Hilfe eines zweidimensionalen Drift-Diffusionsmodells

Zusammenfassung

Ammoniak-sensitive Polymere können als isolierendes Material in organischen Feldeffekttransistoren (OFET) verwendet werden, um Sensoren herzustellen. Experimentelle Resultate zeigten, dass bei gewissen Strukturen (wie zum Beispiel einem dual-gate OFET mit einem ROM-Polymer mit Eosin-Y Gruppe als Isolator) der Strom in Anwesenheit von Ammoniak bei einem speziellen Aufbau um mehr als 800 Prozent steigt. Um dieses Verhalten besser verstehen zu können, wurde der Ladungsträgertransport mit Hilfe eines zweidimensionalen Drift-Diffusions-Modells simuliert. Dafür wurde ein gekoppeltes System bestehend aus Gleichungen der Stromdichten, der Kontinuitäts- und Poissongleichung selbstkonsistent auf einem zweidimensionalen Gitter gelöst. Bevor die Resultate der Simulation mit den Messergebnissen des Experiments verglichen wurden, wurde der Einfluss bestimmter Parameter, wie zum Beispiel der Höhe der Injektionsbarriere, der Mobilität, unterschiedlicher Dielektrizitätskonstanten und des Substratpotentials untersucht. Dann wurde ein bestimmter Satz gerechtfertigter Parameter gewählt, um die I-V-Kurven ohne Anwesenheit von Ammoniak zu berechnen. Schließlich wird anhand dieser Parameter gezeigt, dass die durch den Ammoniak induzierten Änderungen der Charakteristik des OFET von einer Flächenladungsdichte, bestehend aus deprotonierten Hydroxylgruppen, an der Halbleiter-Isolator Grenzfläche stammen.

Contents

1	Introduction	10
2	General Aspects	12
2.1	Organic semiconductors (OSC)	12
2.1.1	Mobility models	13
2.1.2	Potential: the Poisson equation	14
2.1.3	Current density and continuity equations	15
2.1.4	Injection barriers	17
2.2	Organic field-effect transistors	19
2.2.1	Working principle, threshold voltage, operation regimes	20
2.2.2	Dual-gate FET	21
2.3	Sensory mechanism	23
3	Numerical Methods	26
3.1	Gauß-Seidel method	27
3.2	Euler method	28
3.3	Poisson solver	28
3.4	Discretization of the current density and the continuity equation - the Scharfetter-Gummel algorithm	35
3.5	The Algorithm of the simulation	42
4	Results	44
4.1	Experimental results	44
4.2	Simulation studies	48
4.2.1	Parameter studies	49
4.2.2	Comparison of simulation and experiment	58
4.2.3	Optimization of parameters for a device without the presence of ammonia	58
4.2.4	Simulation of the device exposed to ammonia	59

Contents

5	Conclusion	63
6	Acknowledgments	65

List of Figures

2.1	Scheme of σ and π bondings with two carbon atoms in ethene. One of the s orbitals forms a hybrid orbital sp^2 with two p orbitals, while one p orbital stays unchanged. The sp^2 orbitals of the two carbon atoms form a σ bond, while the two remaining p orbitals form a π bond.	12
2.2	Field dependency of the hopping process in OSC. The density of states (DOS) can be described by a Gaussian distribution function depending on the energy ($G(E)$).	13
2.3	Metal/semiconductor contact: (A) energy levels before contacting, (B) after contacting in equilibrium. E_F denotes the Fermi level, E_G the energy of the gap, E_{LUMO} the LUMO level and E_{HOMO} the HOMO level of the OSC. $E_{HOMO,int}$ is the HOMO level of the OSC at the interface to the metal.	17
2.4	The three main different buildups for FET. From left to right: Top-contact-bottom-gate, bottom-contact-bottom-gate and top-gate-bottom-contact	19
2.5	The two regimes and the threshold voltage shown in plot A in an output characteristic and in plot B in a transfer characteristic for a p-type OFET	20
2.6	Three different buildups for dual-gate devices.	22
2.7	Reaction of a ROM-Polymer with a Eosin-Y group and ammonia. The ammonia reacts with the OH -group of the polymer. Thus an ammonium ion and a O^- at the polymer are created.	23
2.8	Principle of the migration of a negative charge through an organic material	24
2.9	Accumulation of negative charges in the dual-OFET used in this thesis. The positive ammonium molecule becomes neutral at the gate.	24
3.1	Cut through an OFET. Reduction from a three dimensional device to two dimensional model. The orange cut is the discretized area, in which the carrier transport will be simulated	26

List of Figures

3.2	Boundary conditions for simulating a dual-gate OFET. The potential at the red dots needs to satisfy the Neumann condition, at the blue dots the Dirichlet condition and at the black dots the potential is calculated and initially chosen arbitrarily.	33
3.3	Beginning of the iterative calculation of the potential. Red dots indicate Neumann conditions, blue dots Dirichlet conditions. Violet x mark the grid points where the potential is calculated while the violet dot indicates a potential that has been calculated. In (A) the potential in the grid point $P_{1,1}$ only depends on the potential given in $P_{1,0}, P_{1,2}$ and $P_{2,1}$, because $\psi_{0,1} = \psi_{2,1}$. In (B) the potential in the next grid point $P_{2,1}$ is calculated with the use of $P_{1,1}$	34
3.4	Boundary conditions for simulating a dual-gate OFET. At the red dots the Neumann condition is applied while at the blue dots the Dirichlet condition is used.	41
3.5	Flowchart of the algorithm	43
4.1	A sketch of the complete design of the device examined.	45
4.2	Transfer characteristics (A) with and (B) without the presence of ammonia at three different drain potentials V_D ($V_D = -25V$ (cross), $-45V$ (circle), $-85V$ (star)).	45
4.3	Comparison of the transfer characteristics with (red) and without (green) the presence of ammonia at the same three different drain potentials $V_D = -25V$ (cross), $-45V$ (circle), $-85V$ (star) in a (A) linear and (B) logarithmic plot	46
4.4	Reduction of the length of the device by relocating the boundaries to reduce computational effort.	48
4.5	Simulation (black) of the device with $V_{SUBS} = 0V$ at $V_D = -25V$ (cross), $V_D = -45V$ (circles) and $V_D = -85V$ (stars) compared to the experimental results (green).	50
4.6	Potential distribution for (A) the initial and (B) the steady state of a single-gate OFET (see text) and (C) the initial and (D) the steady state for the dual-gate device for $V_{SUBS} = 0V$, $V_D = -85V$, $V_G = -85V$. Arrow I depicts the high electric field next to the drain contact, arrow II the region of a low electric field in most of the channel.	51

List of Figures

4.7	Simulation of the increase of the dielectric constant ϵ_r from 6.0 (black) to 6.5 (blue). This is done for three different drain potentials $V_D = -25V$ (cross), $V_D = -45V$ (circles) and $V_D = -85V$ (stars) and compared to the experimental results without the presence of ammonia (green).	52
4.8	Simulation of the increase of the mobility μ_0 from $\mu_0 = 0.4 \times 10^{-6} \frac{m^2}{Vs}$ (black) to $\mu_0 = 0.4 \times 10^{-5} \frac{m^2}{Vs}$ (blue). This is done for three different drain potentials $V_D = -25V$ (cross), $V_D = -45V$ (circles) and $V_D = -85V$ (stars) and compared to the experimental results without (green) and with (red) the presence of ammonia.	53
4.9	Simulation of the change in the injection barrier Δ_h from $\Delta_h = 0.1eV$ (black) to $\Delta_h = 1eV$ (blue). This is done for three different drain potentials $V_D = -25V$ (cross), $V_D = -45V$ (circles) and $V_D = -85V$ (stars) and compared to the experimental results without the presence of ammonia (green).	54
4.10	Impact of the substrate potential V_{SUBS} on the transfer characteristics (blue) for three different drain potentials: $V_D = -25V$ (cross), $-45V$ (circle) and $-85V$ (star). The corresponding substrate potentials are $V_{SUBS} = \frac{V_s - V_D}{2} = -12.5V, -22.5V$ and $-42.5V$. For a better comparison the results for $V_{SUBS} = 0V$ are plotted (black), as well as the experimental results in exposition to ammonia (red).	56
4.11	(A) Potential distribution and (B) hole density of the device for $V_{SUBS} = \frac{V_D + V_s}{2} = -42,5V, V_D = -85V, V_G = -85V$. The substrate potential induces a large electric field at the SiO_x -P3HT interface (arrow III) due to which a second channel is formed (arrow II). Arrow I depicts the gate induced channel.	57
4.12	Simulated transfer characteristics with optimized parameters (Tab. 4.2) compared to the experimental ones without exposure to ammonia (green)	58
4.13	Simulation of the influence of a changed dielectric constant on a transfer characteristic in comparison to the experimental results (red).	60
4.14	Simulation of the influence of the maximum of immobile space charges in the ROM-polymer in comparison to the experimental results (red).	61
4.15	Simulation of the influence of a surface charge density at the P3HT-PVA interface compared to the experimental results in presence of ammonia (red).	62

1 Introduction

Inorganic semi-conducting materials have become increasingly important in today's life. They are used, e.g., in diodes, light emitting devices (LEDs), solar cells and field-effect transistors. With the appearance of organic semiconductors (OSCs) a new advent for these devices has begun. Next to the main advantage of smaller production costs, the different properties of the organic materials lead to new applications, e.g., the creation of flexible devices instead of the rigid inorganic ones and sensors. A great field of research deals with gas-sensory devices. In contrast to non-organic ones, these devices can operate at or near room temperature [1] [2]. There are three main ideas to realize such devices: First, a variation of the mobility can occur in the OSC due to chemical reactions of the gas with the OSC [1]. Second, a chemical reaction in a self-assembled monolayer [3] leads to an increase of the capacitance and, thus, an increase in the current. Third, the gas can react with the isolating material and change the capacitance and, consequently, the current. One of those devices, a sensory organic field-effect transistor (OFET), which has been built by A. Klug and his coworkers [2], is the main subject of this thesis.

This device is highly sensitive to ammonia, due to a layer consisting of a ROM-polymer with an Eosin-Y-group attached [4]. Although the OSC used (P3HT) reacts with ammonia upon which its mobility is decreased [5], experimental measurements showed that the current increases by more than 800% under exposure of ammonia. Three main scenarios have been put forward to explain this effect:

- Change in the dielectric constant: The dielectric constant of the ROM-polymer (ROMP) is changed due to the interaction of the Eosin-Y-group with the ammonia. Experimental measurements of the dielectric constant of this material showed an increase of $\epsilon_{ROM-polymer}$ from 6.0 to 6.5 [2]. This gives rise to an increase in the capacitance and, therefore, to an increase of the current.
- Formation of a constant space charge density in the ROM-polymer: Positively charged ammonium molecules and negatively charged O⁻-groups are created due to the reaction of the ammonia molecules with the polymer. While the positive

ammonium molecules migrate to the negatively charged gate contact, the negatively charged O^- -groups are immobile and create a charge density in the polymer. Like the change in the dielectric constant, this results in a higher capacitance and, in consequence, in an increase of the current.

- Formation of a surface charge layer at the interface between the isolating material and the OSC: Rather than remaining fixed, the negative charges travel through the device and accumulate at the interface to the OSC. The resulting surface charge density increases the capacitance and, thus, also the current.

As it is very difficult to verify a particular scenario via experimental methods, complementary simulations are necessary. For this purpose, a two dimensional drift-diffusion model is developed that is suitable to simulate the complete device.

This thesis is structured as follows: After this introduction, the second chapter gives a survey on the properties, characteristics, and phenomena observed in OSCs (section 2.1), OFETs (section 2.2), as well as sensors with particular focus on the properties that form the basis of sensing of this device (section 2.3).

The third chapter deals with the numerical methods used to simulate the device. There, the continuity and the current density equations are combined with the Poisson equation, leading to a system of equations that is solved self-consistently on a two-dimensional non-regular grid.

The first section of chapter 4 is dedicated to the experimental data. Different experimentally measured characteristics are compared and a tentative explanation of the observed effects is given. Section 4.2 is divided into two parts: In the first one, parameters studies are made (subsection 4.2.1). This is done in order to understand the influence of the most important parameters on the transfer characteristics. These parameters are the dielectric constant of the isolating ROM-polymer, the mobility, the injection barrier and the substrate potential. In subsection 4.2.2, the three scenarios, each of which could give rise to an NH_3 sensitivity, are tested by choosing a corresponding set of parameters and model extensions.

In the conclusion section (chapter 5), the results are then summarized and a sensing mechanism is proposed.

2 General Aspects

First, a short survey is given about the material properties of organic semiconductors. These materials are used in many organic devices, e. g. in organic field-effect transistors (OFET) (2.2). By using certain sensoric materials these OFETs can be built as sensoric devices, explained shortly in the last section of this chapter.

2.1 Organic semiconductors (OSC)

The basic properties of OSC are well known. They rely on the conjugated π -electron system, resulting from an sp^2 hybridization of carbon compounds [6]. The most simple example for such a hybridization is that of ethene, as shown in Fig. 2.1.

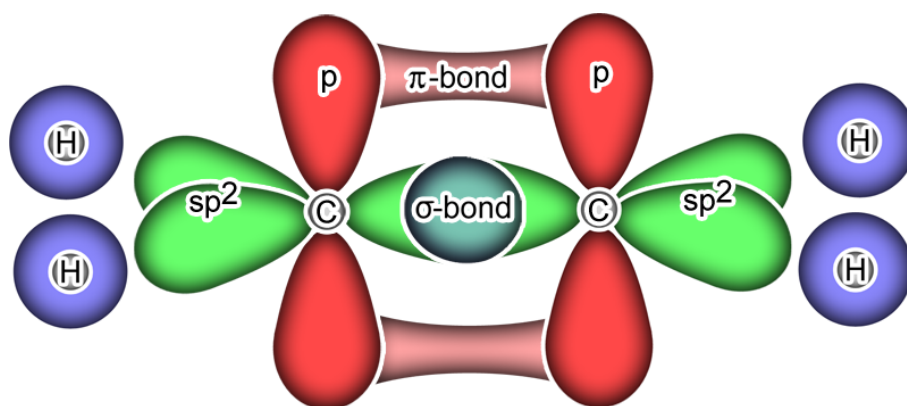


Figure 2.1: Scheme of σ and π bondings with two carbon atoms in ethene. One of the s orbitals forms a hybrid orbital sp^2 with two p orbitals, while one p orbital stays unchanged. The sp^2 orbitals of the two carbon atoms form a σ bond, while the two remaining p orbitals form a π bond.

While the σ -type orbitals are localized between the carbon atoms, the delocalized π -type orbitals have a weak overlap and therefore low binding energies, leading to delocalized molecular orbitals. This is exploited in conjugated polymers, where the delocalization of the π bonds leads to intrinsic conductivity. Although not yet fully understood,

it is clear that the transport mechanism differs in many respects from inorganic materials. While it is possible to describe most inorganic semiconductor as one perfect molecule with well defined crystal topography, organic materials often occur as disordered solid containing countless independent molecules with different orientation and connection to each other. This topography has an important effect on the mobility of the charge carriers in OSCs. These mechanisms regarding the mobility of the organic semiconducting material are addressed in section 2.1.1

Albeit the above mentioned differences, there is nonetheless also a similarity between these two materials. As in inorganic semiconductors, there is also a kind of band gap between the highest occupied molecular orbital (called HOMO, similar to the edge of the valance band in inorganic materials) and the lowest unoccupied molecular orbital (called LUMO, being more or less the edge of the conduction band). The gap between these two levels is in the range of some 100 meV [6]. This value is not well defined due to the nature of the organic semiconductor and its morphology. Due to disorder, the resulting energy levels of the material form a Gaussian density of states (DOS) (Fig. 2.2).

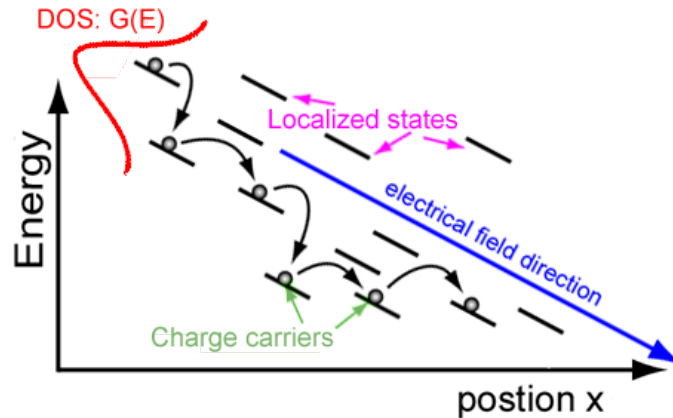


Figure 2.2: Field dependency of the hopping process in OSC. The density of states (DOS) can be described by a Gaussian distribution function depending on the energy ($G(E)$.)

2.1.1 Mobility models

The mobility μ of the charge carriers in an OSC depends on two main processes: the intrachain and the interchain charge carrier transport. The former one consists of the transport in a single molecule, where long conjugation lengths lead to a high mobility.

The later covers the hopping process from one chain of carbon molecules to the other. The charge carriers must overcome a so called hopping barrier.

In contrast to most inorganic semiconductors, the transport is not phonon-limited, but rather phonon-assisted. This results in a higher energy of the charge carriers, which allows an easier penetration of barriers [7]. In addition to the high temperature, dependence the mobility is also electric field-dependent in semiconducting materials as can be seen in Fig. 2.2 [8] [9]. This is reflected by a lot of different models [10] [11] [12]. In the following, only the density-dependent model is presented, due to the high concentration differences observed in OFETs. Miller-Abrahams described the hopping probability from one chain to another as a process thermally associated by acoustic phonons in a Gaussian energy landscape [13]. The equation was solved by Pasveer et al. for hopping of carriers on a cubic lattice [11]. Their final result for a density dependent mobility $\mu(p)$ leads to

$$\mu(p) = \mu_0 \exp \left[\frac{1}{2} (\hat{\sigma}^2 - \hat{\sigma}) \left(\frac{2p}{N_V} \right)^\delta \right] \quad (2.1)$$

with

$$\delta = 2 \frac{\ln(\hat{\sigma}^2 - \hat{\sigma}) - \ln(\ln 4)}{(\hat{\sigma}^2)} \quad (2.2)$$

Here, μ_0 denotes the mobility at zero concentrations of the charge carriers, $\hat{\sigma}$ the width of the Gaussian density of states (DOS) and p the density distribution of the charge carriers. N_V is the effective density of states in the valence band and defined by

$$N_V = 2 \left[2 \frac{2\pi m_p^* k_B T}{\hbar^2} \right]^{\frac{3}{2}} \quad (2.3)$$

with the Boltzmann constant k_B , the reduced Planck constant \hbar and m_p^* denoting the effective mass of the charge carrier [14, page 19]. For disordered solids, instead of N_V an effective density of states for organic materials N_{HOMO} must be used here. Although not clearly defined, this parameter is handled as fit-parameter in simulations for different materials, e. g. performed by Torricelli et al. for P3HT [15]. Therefore, estimations can be given.

2.1.2 Potential: the Poisson equation

As mentioned before, the electric field \mathbf{E} is of great importance for the charge transport in OSCs. The field itself is connected with the electrostatic potential ψ in the domain

2 General Aspects

$\Omega \subset \mathbb{R}^3$ via

$$\mathbf{E}(\mathbf{r}) = -\nabla\psi(\mathbf{r}) \quad \mathbf{r} \in \Omega \quad (2.4)$$

The Gauß's law is given by

$$\nabla \cdot \mathbf{D}(\mathbf{r}) = \rho(\mathbf{r}) \quad \mathbf{r} \in \Omega \quad (2.5)$$

where ρ is the total charge density and \mathbf{D} is the electric displacement field, which depends on the electric field by

$$\mathbf{D}(\mathbf{r}) = \epsilon_0\epsilon_r\mathbf{E}(\mathbf{r}) \quad \mathbf{r} \in \Omega \quad (2.6)$$

Inserting (2.4) and (2.6) into (2.5) leads to the Poisson equation

$$\nabla \cdot (\epsilon_0\epsilon_r(\mathbf{r})\nabla\psi(\mathbf{r})) = -\rho(\mathbf{r}) \quad \mathbf{r} \in \Omega \quad (2.7)$$

with ϵ_0 denoting the absolute permittivity and ϵ_r the relative permittivity. It relates the electrostatic potential ψ with the total charge density ρ , which contains the contribution from mobile carriers as well as possible fixed charge distributions, be that space- or surface-charge densities. The Poisson equation can be solved by taking into account Neumann and/or Dirichlet boundary conditions:

$$\text{Dirichlet :} \quad \psi(\mathbf{r}) = g(\mathbf{r}) \quad \mathbf{r} \in \partial\Omega \quad (2.8)$$

$$\text{Neumann :} \quad \frac{\partial\psi(\mathbf{r})}{\partial\mathbf{n}} = f(\mathbf{r}) \quad \mathbf{r} \in \partial\Omega \quad (2.9)$$

where $f(\mathbf{r})$ and $g(\mathbf{r})$ are a given scalar functions and \mathbf{n} denotes the normal to the given boundary $\partial\Omega$.

2.1.3 Current density and continuity equations

The two main driving forces behind the motion of charge carriers are the drift and the diffusion. While the drift is caused by the electric field \mathbf{E} , the diffusion is driven by the gradient of the charge carrier density ∇p for positively and ∇n for negatively charged

2 General Aspects

carriers [16]. In the domain $\Omega \subset \mathbb{R}^3$, the two corresponding current densities read:

$$\begin{aligned}\mathbf{J}_p(\mathbf{r}, t) &= qp(\mathbf{r}, t)\mu_p(\mathbf{r})\mathbf{E}(\mathbf{r}) - qD_p(\mathbf{r}, t)\nabla p(x, y) \quad \mathbf{r} \in \Omega \\ \mathbf{J}_n(\mathbf{r}, t) &= qn(\mathbf{r}, t)\mu_n(\mathbf{r})\mathbf{E}(\mathbf{r}) + qD_n(\mathbf{r})\nabla n(\mathbf{r}, t) \quad \mathbf{r} \in \Omega\end{aligned}\tag{2.10}$$

Here, q is the elementary charge, while $\mu_{p/n}(\mathbf{r})$ stands for the mobility for positively/negatively charged carriers. $D_{p/n}(\mathbf{r})$ denotes the diffusion constant, calculated by the Einstein relation:

$$D_p(\mathbf{r}) = \frac{\mu_p(\mathbf{r})k_B T}{q} \quad \mathbf{r} \in \Omega\tag{2.11}$$

$$D_n(\mathbf{r}) = \frac{\mu_n(\mathbf{r})k_B T}{q} \quad \mathbf{r} \in \Omega\tag{2.12}$$

where k_B is the Boltzmann constant and T the Temperature.

The current-density equations (2.10) are coupled with the continuity equations

$$\begin{aligned}\frac{1}{q}\nabla \cdot \mathbf{J}_p(\mathbf{r}, t) + \frac{\partial p(\mathbf{r}, t)}{\partial t} &= G(\mathbf{r}) \quad \mathbf{r} \in \Omega \\ -\frac{1}{q}\nabla \cdot \mathbf{J}_n(\mathbf{r}, t) + \frac{\partial n(\mathbf{r}, t)}{\partial t} &= G(\mathbf{r}) \quad \mathbf{r} \in \Omega\end{aligned}\tag{2.13}$$

with $G(\mathbf{r})$ being the generation rate.

These equations can be solved by taking into account Neumann and/or Dirichlet boundary conditions:

$$\text{Dirichlet :} \quad p(\mathbf{r}, t) = g(\mathbf{r}) \quad \mathbf{r} \in \partial\Omega\tag{2.14}$$

$$\text{Neumann :} \quad \frac{\partial J(\mathbf{r}, t)}{\partial \mathbf{n}} = f(\mathbf{r}) \quad \mathbf{r} \in \partial\Omega\tag{2.15}$$

where $f(\mathbf{r})$ and $g(\mathbf{r})$ are a given scalar functions and \mathbf{n} denotes the normal to the given boundary $\partial\Omega$.

2.1.4 Injection barriers

The work function $q\phi_m$ of gold is 5.1eV and the electron affinity $q\chi_S$ of P3HT (the OSC used in the devices examined) is 3.5eV [17]. In thermal equilibrium, the Fermi levels of two contacted materials must be the same. This is shown in Fig. 2.3. The bending of

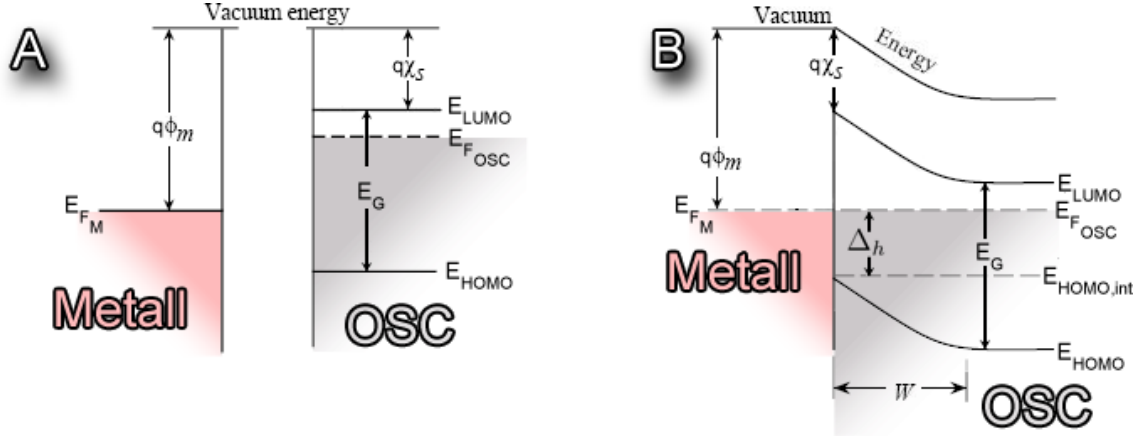


Figure 2.3: Metal/semiconductor contact: (A) energy levels before contacting, (B) after contacting in equilibrium. E_F denotes the Fermi level, E_G the energy of the gap, E_{LUMO} the LUMO level and E_{HOMO} the HOMO level of the OSC. $E_{HOMO,int}$ is the HOMO level of the OSC at the interface to the metal.

the energy levels will be neglected as its width and height are assumed to be very small compared to the size of the OSC and its energy levels.

As positively charged carriers from the metal enter the OSC, an injection barrier Δ_h can be defined by the difference between the Fermi level (E_F) and the energy of the HOMO of the OSC at the interface ($E_{HOMO,int}$) as seen in Fig. 2.3:

$$\Delta_h = E_G - q(\phi_M - \chi_S) \quad (2.16)$$

With a given effective density of states associated to the HOMO level (N_{HOMO}) the density of charge carriers at the contact $p_{contact}$ can be calculated, when assuming a non-degenerate semiconductor in thermal equilibrium [14, page 157]:

$$p_{contact} = N_{HOMO} \exp\left(-\frac{\Delta_h}{k_B T}\right) \quad (2.17)$$

with k_B denoting the Boltzmann constant and N_{HOMO} the effective density of states for organic materials introduced in 2.1.1. Although thermal equilibrium is not fully reached in an actual device, this model is a good estimation for the simulation, as here the charge

2 General Aspects

carrier density depends only on the injection barrier and the density of states and not on other factors, e. g., time, potential or charge carriers in the device. It can be used to incorporate Dirichlet conditions (Eq. (2.14)) at the contacts in the simulation.

2.2 Organic field-effect transistors

There are several advantages for using organic materials compared to inorganic materials in electronic devices. The main reasons are that organic materials are cheaper than their inorganic counterparts and that, due to their organic nature, they allow even flexible devices. Most of the devices are produced by spin-coating, where an excess amount of a solution containing the OSC is placed on substrate, which is rotated at high speed in order to spread the fluid by centrifugal force. Other production methods include painting or printing on the used substrate.

One of the devices where OSCs are used are organic field-effect transistors. Here, the semi-conducting material is made of an organic substance, whereas the rest of the device can be organic or inorganic. There are mostly three different designs as shown in Fig. 2.4 although other geometries can be imagined. The most simple one of these devices is the top-contact-bottom-gate OFET. There, the gate is also the substrate, on top of which the isolator and the OSC are placed. Drain and source are connected only to the OSC and are located on top of the device. In a bottom-contact-bottom-gate OFET the setup is similar, but source and drain are placed on top of the isolator, before the OSC is applied. So the two electrodes are covered by the OSC. In a top-gate-bottom-contact OFET source and drain are placed on a certain substrate and covered by the OSC similar to the bottom-contact-bottom-gate device. The isolator is placed on top of the OSC and the gate is located on top of the isolator.

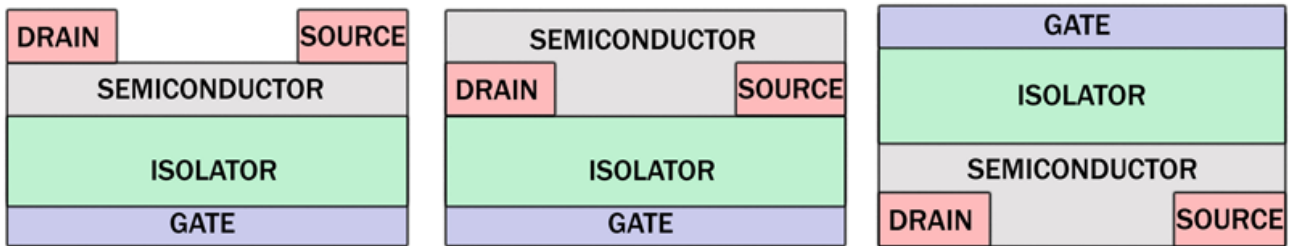


Figure 2.4: The three main different buildups for FET. From left to right: Top-contact-bottom-gate, bottom-contact-bottom-gate and top-gate-bottom-contact

The thickness of the active material is some 10 nm, while that of the dielectric material is more than 100 nm. Their width is a few millimeters. The length of the channel of a typical OSC is between 10 μm and 100 μm , while the length of the contacts varies from a few micrometer to some millimeter. The contacts are mostly made of gold or silver. Their Fermi levels are close to the HOMO-level of the OSCs. This property and the unintentional doping of the used OSCs is the reason why this thesis will only refer

to transistors with positive charge carriers (holes) [18]. Negative charge carriers will be neglected, although OFETs with negative charge carriers have been realized too.

2.2.1 Working principle, threshold voltage, operation regimes

The gate influences the electric field between source and drain. Normally the voltage at the gate is set so that additional mobile charge carriers can enter the device through the source and accumulate at the interface between the OSC and the dielectric material. This accumulation region is called the channel. For p-type transistors, it is valid that the lower the gate potential the more positive charge carriers enter and leave the device, thus creating a higher current. Another effect that increases the current is the hole-density dependence of the mobility. If there are more charge carriers in the channel, the mobility rises (Eq. 2.1) and also the current (Eq. 2.10).

If the gate voltage is set above a certain value, no additional mobile charge carriers can enter the device and no channel is formed. The charge density in the bulk is the same as at the interface. This gate voltage is called the threshold voltage. This is also the voltage at which the conductance of the interface exceeds that of the bulk, because above the threshold voltage only the conductance of the bulk determines the current. When no fixed charges are present in an OFET the threshold voltage is zero [18].

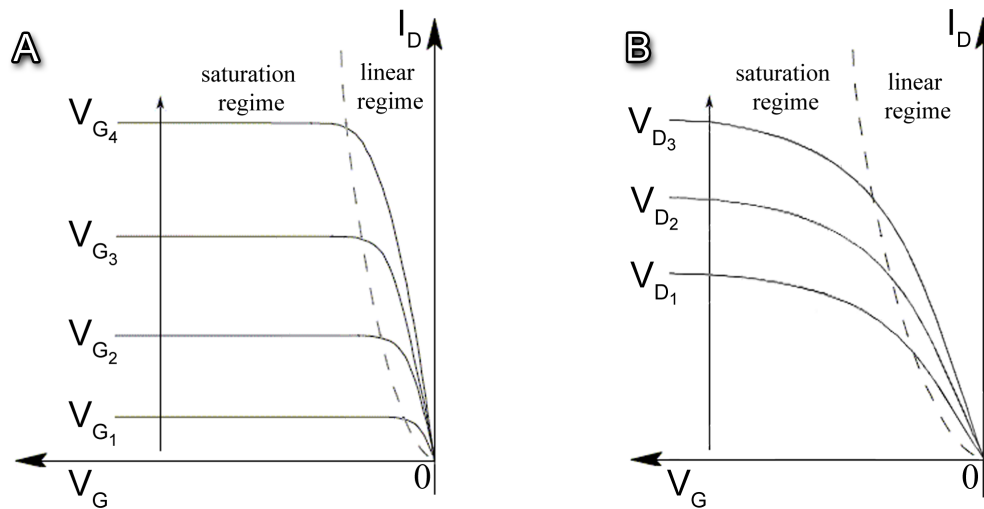


Figure 2.5: The two regimes and the threshold voltage shown in plot A in an output characteristic and in plot B in a transfer characteristic for a p-type OFET

The current at the drain depends on two main parameters: the potentials applied at the drain contact and the gate contact. The first correlation is illustrated by a so called output characteristic, the second one by a transfer characteristic. In Fig 2.5 examples

of such characteristics are shown. As can be seen, these curves can be divided into two parts: The linear regime and the saturation regime (Fig. 2.5). The linear regime is defined as the part of the transfer characteristic where the gate voltage V_G is between the drain voltage V_D and the threshold voltage V_{th} . When V_G is also below V_D then it is called saturation regime. The current at the drain $I_{d,lin}$ for the linear regime and $I_{d,sat}$ for the saturation regime can be approximated by [14, pages 303-306]

$$I_{d,lin} = \frac{W}{L} \mu C_i \left[(V_G - V_{th}) V_D - \frac{V_D^2}{2} \right] \quad \text{for} \quad V_G > V_D \quad (2.18)$$

$$I_{d,sat} = \frac{W}{2} L \mu C_i (V_G - V_{th})^2 \quad \text{for} \quad V_G < V_D \quad (2.19)$$

Here, W is the width and L the length of the channel, while C_i is the capacitance of the insulator, and μ denotes the mobility of the charge carriers.

In the linear regime, the current is proportional to the gate voltage (Eq. (2.18)). In the saturation regime, the current is independent of the drain voltage and depends quadratically on the gate voltage. These assumptions are correct for OFETs with much longer channel length than its width and for constant mobilities μ . The first condition is usually fulfilled in OFETs (vide supra), while the mobility is field-dependent, dependent on morphology and concentration of charge carriers. Consequently, the mobility is not uniform in the active region. Although realistic results will deviate from these equations, they give a good approximation and are frequently used to extract parameters such as the threshold voltage and mobility.

2.2.2 Dual-gate FET

As shown in next sections, the structure of the device investigated in this thesis is reminiscent of a dual-gate FET. This is obtained when two FETs are combined in one device [19]. There are three principle buildups as shown in Fig. 2.6.

In such a device, the electric field and, therefore, the current between source and drain depends on the voltage applied to both gates. If one of the gates operates at a voltage above the threshold voltage, the occurring transfer characteristic is similar to that of a normal OFET with one gate. If both operate below the threshold voltage, the occurring transfer characteristic is a mix of both of these two transfer characteristics related to the separated gates [20]. This is due to the fact that each gate creates its own channel.

2 General Aspects

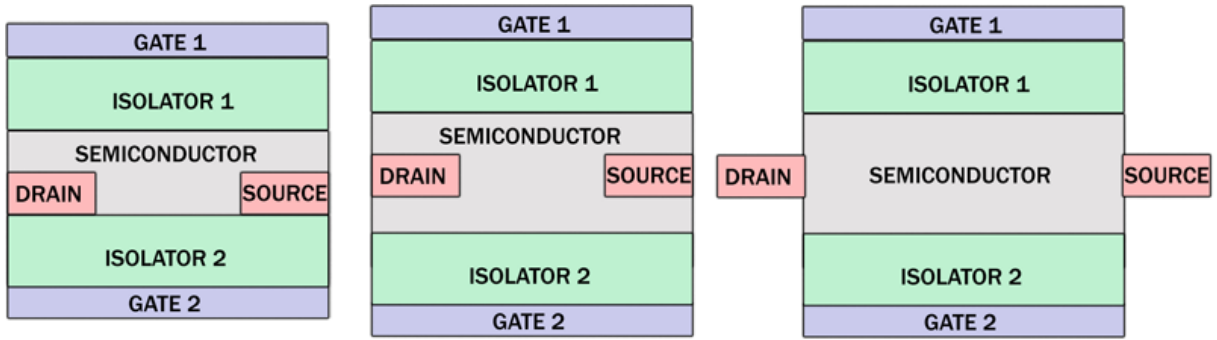


Figure 2.6: Three different buildups for dual-gate devices.

Two channels are formed, one at the top of the semi-conducting material and one at the bottom. The current of both of the channels add to the observed transfer characteristic.

2.3 Sensory mechanism

Sensors are defined as devices made of materials altering their physical properties after reacting with another substance. This change results in a signal which can be measured by an instrument or by an observer.

The sensory material considered in this thesis is a ROM-polymer used as isolator in an OFET, which reacts with ammonia due to its Eosin-Y group. This reaction is described in Fig. 2.7. The neutral ammonia molecule reacts with the OH-group of the Eosin-Y at the polymer. Experimental results showed a significant increase of the current by more than 800% when exposed to ammonia. Three different scenarios are conceivable

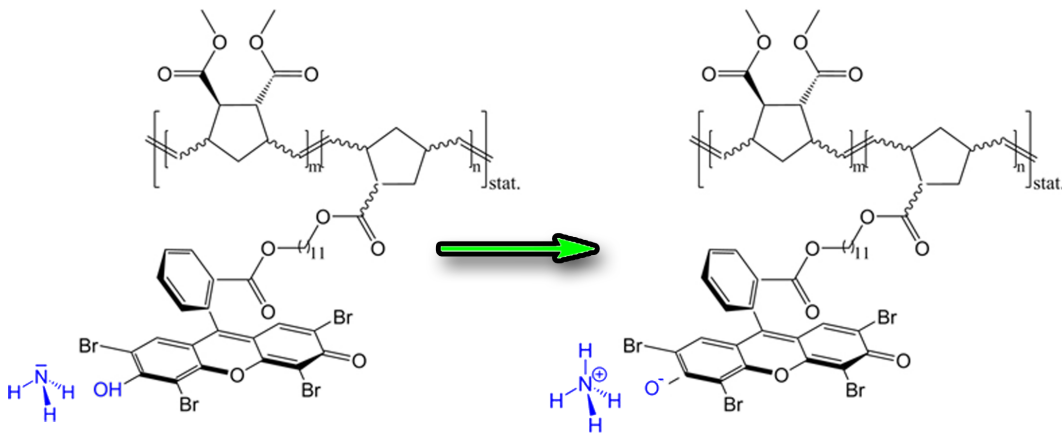


Figure 2.7: Reaction of a ROM-Polymer with a Eosin-Y group and ammonia. The ammonia reacts with the *OH*-group of the polymer. Thus an ammonium ion and a O^- at the polymer are created.

to explain the observed effect:

Change in the dielectric constant: The dielectric constant of the ROM-polymer is changed due to the interaction of the Eosin-Y-group with the ammonia. Measurements of the dielectric constant of this material showed an increase of $\epsilon_{ROM-polymer}$ from 6.0 to 6.5 [2]. This results in an increase in the capacitance measurements and, therefore, it leads to an increase of the current.

Formation of a constant space charge density in the ROM-polymer: While the ammonium ion migrates to the negatively charged gate electrode of the OFET, and there supposedly becoming neutral again or dissolving, the O^- stays bound to the polymer.

Thus, a homogeneous negative charge density could be created in the polymer. As in case of a change in the dielectric constant, this results in a higher capacitance and, consequently, leads to an increase of the current.

Formation of a surface charge layer at the interface between the isolating material and the OSC: The negatively charged O^- -group attracts the partially positive charged H -atom of the neighboring OH -group. This H -atom can now move to the O^- , forming a new σ -bond and therefore transferring the negative charge to the other oxygen atom. The principle is shown in Fig. 2.8 [21]. A polyvinyl alcohol (PVA) layer has to be

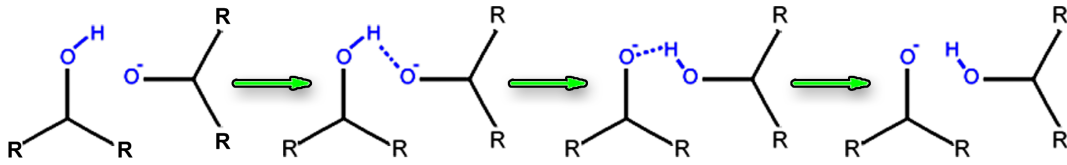


Figure 2.8: Principle of the migration of a negative charge through an organic material

located between the ROM-Polymer and the OSC due to production issues. As the name suggests, the concentration of OH -groups in the PVA is much higher than in the ROM-polymer. Hence, negative charges produced in the ROM-polymer and located near the interface to the PVA can easily migrate through it, with a motion pattern shown in Fig. 2.8. There, they accumulate at the boundary to the OSC (Fig. 2.9). In this case the

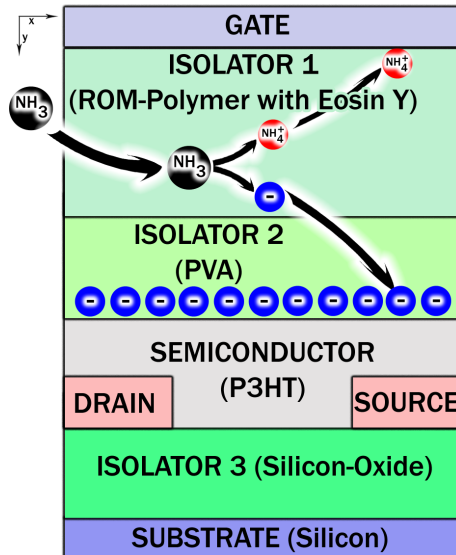


Figure 2.9: Accumulation of negative charges in the dual-OFET used in this thesis. The positive ammonium molecule becomes neutral at the gate.

2 General Aspects

OSC is P3HT, which is a substance that is highly unlikely to support the transport of the negative charges. Next to a change in the dielectric constant, this accumulation of the negative charges at the interface to the OSC is supposed to result in a change of the current.

In order to analyze these scenarios, a simulation tool must be implemented, that is capable of dealing with the special geometry of the device and that is also capable of incorporating these three proposed mechanisms. The results of the simulation are then compared to the experimental ones in order to identify the origin of the NH_3 sensitivity.

3 Numerical Methods

The properties and phenomena discussed in the previous section must now be modeled in a way, which allows us to simplify the carrier transport in the device. As the device is assumed to be infinitely extended in z-direction, the physically three-dimensional problem can be reduced to a two-dimensional one from a mathematical point of view.

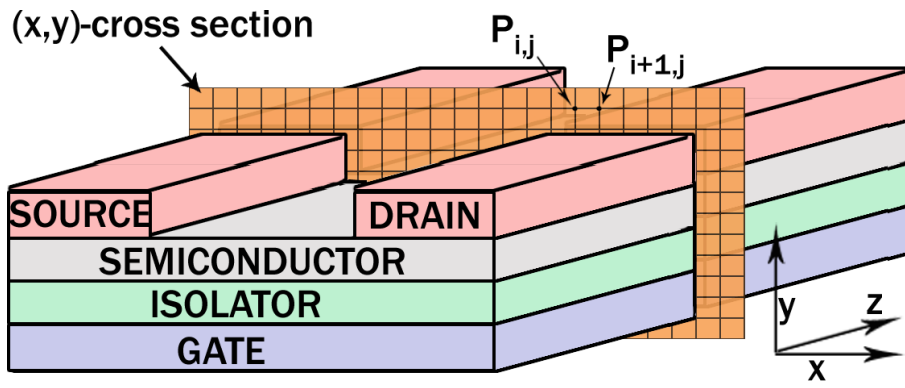


Figure 3.1: Cut through an OFET. Reduction from a three dimensional device to two dimensional model. The orange cut is the discretized area, in which the carrier transport will be simulated

In order to solve the problem numerically, the (x,y)- cross section area of the transistor must be discretized by a grid. The resulting grid points are of the form

$$P_{i,j} = (x_i, y_j) \tag{3.1}$$

with $i = 0, 1, \dots, N$ and $j = 0, 1, \dots, M$ are defined by

$$\begin{aligned} x_0 &= 0, & x_{i+1} &= x_i + \Delta x_i, & i &= 0, 1, \dots, M - 1 \\ y_0 &= 0, & y_{j+1} &= y_j + \Delta y_j, & j &= 0, 1, \dots, N - 1 \end{aligned} \tag{3.2}$$

3.1 Gauß-Seidel method

Considering a square system of linear equations $\mathbf{Ax} = \mathbf{b}$ with the matrix $\mathbf{A} \in \mathbb{C}^{n \times n}$, the vector of unknowns $\mathbf{z} \in \mathbb{C}^n$ and the inhomogeneity $\mathbf{b} \in \mathbb{C}^n$:

$$A = \begin{bmatrix} a_{11} & a_{12} & \cdots & a_{1n} \\ a_{21} & a_{22} & \cdots & a_{2n} \\ \vdots & \vdots & \ddots & \vdots \\ a_{n1} & a_{n2} & \cdots & a_{nn} \end{bmatrix}, \quad \mathbf{x} = \begin{bmatrix} x_1 \\ x_2 \\ \vdots \\ x_n \end{bmatrix}, \quad \mathbf{b} = \begin{bmatrix} b_1 \\ b_2 \\ \vdots \\ b_n \end{bmatrix} \quad (3.3)$$

The matrix \mathbf{A} is split in two triangular matrices

$$\mathbf{A} = \mathbf{L} + \mathbf{U}$$

with the lower triangular matrix $\mathbf{L} \in \mathbb{C}^{n \times n}$ and the strictly upper triangular matrix $\mathbf{U} \in \mathbb{C}^{n \times n}$:

$$\mathbf{L} = \begin{bmatrix} a_{11} & 0 & \cdots & 0 \\ a_{21} & a_{22} & \cdots & 0 \\ \vdots & \vdots & \ddots & \vdots \\ a_{n1} & a_{n2} & \cdots & a_{nn} \end{bmatrix}, \quad \mathbf{U} = \begin{bmatrix} 0 & a_{12} & \cdots & a_{1n} \\ 0 & 0 & \cdots & a_{2n} \\ \vdots & \vdots & \ddots & \vdots \\ 0 & 0 & \cdots & 0 \end{bmatrix} \quad (3.4)$$

Now the system can be rewritten by

$$\mathbf{Lx} = \mathbf{b} - \mathbf{Ux} \quad (3.5)$$

The Gauß-Seidel method is an iterative method, where the vector \mathbf{x} on the left hand side of the equation is obtained by using its previous value \mathbf{x} on the right hand side. Beginning with the starting value \mathbf{x}^0 the $(k+1)$ -th iteration of the equation reads:

$$\mathbf{x}^{(k+1)} = \mathbf{L}^{-1}(\mathbf{b} - \mathbf{Ux}^{(k)}) \quad (3.6)$$

By taking advantage of the triangular form of \mathbf{L} , the elements of $x^{(k+1)}$ can be computed sequentially using forward substitution:

$$x_i^{(k+1)} = \frac{1}{a_{ii}} \left(b_i - \sum_{j>i} a_{ij} x_j^{(k)} - \sum_{j<i} a_{ij} x_j^{(k+1)} \right), \quad i = 1, 2, \dots, n \quad (3.7)$$

This procedure is continued until it is regarded to be converged when $|x_i^{(k+1)} - x_i^k| < \eta$, with a predefined limit η .

3.2 Euler method

The Euler method is a method to discretize time dependent problems,

$$\frac{dy}{dt} = f(t, y(t)), \quad y(t_0) = y_0 \quad (3.8)$$

by using the first two terms of the Taylor expansion of y , which represent a linear approximation around the point $(t, y(t))$:

$$y(t+h) = y(t) + hf(t, y(t)) + O(t^2) \quad (3.9)$$

The error of this approximation is of $O(t^2)$. Assuming that discrete time steps are used, beginning with t_0 the n -th time step can be estimated by the following equation:

$$y(t_{n+1}) = y_n + hf(t_n, y_n) \quad (3.10)$$

The problem with this explicit Euler method is that it is unstable for large time steps.

A different method is the implicit or backward Euler method. Instead of the Taylor expansion used in Eq. (3.9) the problem is approximated by:

$$y(t) = y(t-h) + hf(t, y(t)) + O(t^2) \quad (3.11)$$

Thus getting

$$y(t_{n+1}) = y_n + hf(t_{n+1}, y_{n+1}) \quad (3.12)$$

The implicit version is more difficult to solve, since a system of linear equations needs to be solved at each time step, but it allows the use of much larger time steps.

3.3 Poisson solver

The first equation to be discretized is the Poisson equation mentioned in section 2.1.2. The form of the equation in (2.7) is used to determine the electrostatic potential in the case of a position-dependent permittivity:

$$\nabla \cdot (\epsilon_0 \epsilon_r(x, y) \nabla \psi(x, y)) = -\rho(x, y) \quad (x, y) \in \Omega \quad (3.13)$$

3 Numerical Methods

In two dimensions, this equation can be written as

$$\nabla \cdot \mathbf{f}(x, y) = \nabla \cdot (f_x(x, y), f_y(x, y)) = \frac{\partial f_x(x, y)}{\partial x} + \frac{\partial f_y(x, y)}{\partial y} = -\rho(x, y) \quad (3.14)$$

where f_x and f_y are the two components of the the vector field defined by

$$\mathbf{f}(x, y) = \epsilon_0 \epsilon_r(x, y) \nabla \psi(x, y) = \epsilon_0 \epsilon_r(x, y) \left(\frac{\partial \psi(x, y)}{\partial x}, \frac{\partial \psi(x, y)}{\partial y} \right) \quad (3.15)$$

The Taylor expansion of $f_x(x, y)$ truncated after the second term at $x_i + \frac{1}{2}\Delta x_i = x_{i+\frac{1}{2}}$ and $x_i - \frac{1}{2}\Delta x_{i-1} = x_{i-\frac{1}{2}}$ reads:

$$f_x(x_{i+\frac{1}{2}}, y_j) = f_x(x_i, y_j) + \frac{1}{2}\Delta x_i \frac{\partial f_x(x, y)}{\partial x} \Big|_{x_i, y_j} + O(x^2) \quad (3.16)$$

$$f_x(x_{i-\frac{1}{2}}, y_j) = f_x(x_i, y_j) - \frac{1}{2}\Delta x_{i-1} \frac{\partial f_x(x, y)}{\partial x} \Big|_{x_i, y_j} + O(x^2) \quad (3.17)$$

Neglecting the error of $O(x^2)$ and subtracting Eq. (3.17) from Eq. (3.16) yields

$$f_x(x_{i+\frac{1}{2}}, y_j) - f_x(x_{i-\frac{1}{2}}, y_j) = \frac{(\Delta x_i + \Delta x_{i-1})}{2} \frac{\partial f_x(x, y)}{\partial x} \Big|_{x_i, y_j} \quad (3.18)$$

which results in

$$\frac{f_x(x_{i+\frac{1}{2}}, y_j) - f_x(x_{i-\frac{1}{2}}, y_j)}{\frac{1}{2}(\Delta x_i + \Delta x_{i-1})} = \frac{\partial f_x(x, y)}{\partial x} \Big|_{x_i, y_j} \quad (3.19)$$

A similiar procedure for $f_y(x, y)$ leads to:

$$\frac{f_y(x_i, y_{j+\frac{1}{2}}) - f_y(x_i, y_{j-\frac{1}{2}})}{\frac{1}{2}(\Delta y_j + \Delta y_{j-1})} = \frac{\partial f_y(x, y)}{\partial y} \Big|_{x_i, y_j} \quad (3.20)$$

Inserting Eq. (3.19) and Eq. (3.20) into Eq. (3.14) results in the finite differences approximation for the divergence of a vector field $\mathbf{f}(x, y)$ with an error of $O(x^2) + O(y^2)$:

$$\nabla \cdot \mathbf{f}(x, y) \Big|_{x_i, y_j} = \frac{f_x(x_{i+\frac{1}{2}}, y_j) - f_x(x_{i-\frac{1}{2}}, y_j)}{\frac{1}{2}(\Delta x_i + \Delta x_{i-1})} + \frac{f_y(x_i, y_{j+\frac{1}{2}}) - f_y(x_i, y_{j-\frac{1}{2}})}{\frac{1}{2}(\Delta y_j + \Delta y_{j-1})} \quad (3.21)$$

3 Numerical Methods

Reinserting Eq. (3.15) into Eq. (3.21) yields

$$\begin{aligned} \nabla \cdot (\epsilon_0 \epsilon_r(x, y) \nabla \psi(x, y))|_{(x_i, y_j)} &= \epsilon_0 \frac{\left[\epsilon_r(x, y) \frac{\partial \psi(x, y)}{\partial x} \right]_{x_{i+\frac{1}{2}}, y_j} - \left[\epsilon_r(x, y) \frac{\partial \psi(x, y)}{\partial x} \right]_{x_{i-\frac{1}{2}}, y_j}}{\frac{1}{2}(\Delta x_i + \Delta x_{i-1})} \\ &+ \epsilon_0 \frac{\left[\epsilon_r(x, y) \frac{\partial \psi(x, y)}{\partial y} \right]_{x_i, y_{j+\frac{1}{2}}} - \left[\epsilon_r(x, y) \frac{\partial \psi(x, y)}{\partial y} \right]_{x_i, y_{j-\frac{1}{2}}}}{\frac{1}{2}(\Delta y_j + \Delta y_{j-1})} \end{aligned} \quad (3.22)$$

Using the notation

$$[f(x, y)g(x, y)]_{i,j} = f_{i,j}g_{i,j} \quad (3.23)$$

as well as the approximations

$$\begin{aligned} \left[\frac{\partial \psi(x, y)}{\partial x} \right]_{x_{i-\frac{1}{2}}, y_j} &= \frac{\psi_{i,j} - \psi_{i-1,j}}{\Delta x_{i-1}} & \left[\frac{\partial \psi(x, y)}{\partial x} \right]_{x_{i+\frac{1}{2}}, y_j} &= \frac{\psi_{i+1,j} - \psi_{i,j}}{\Delta x_i} \\ \left[\frac{\partial \psi(x, y)}{\partial y} \right]_{x_i, y_{j-\frac{1}{2}}} &= \frac{\psi_{i,j} - \psi_{i,j-1}}{\Delta y_{j-1}} & \left[\frac{\partial \psi(x, y)}{\partial y} \right]_{x_i, y_{j+\frac{1}{2}}} &= \frac{\psi_{i,j+1} - \psi_{i,j}}{\Delta y_j} \end{aligned}$$

leads to

$$\begin{aligned} \nabla \cdot (\epsilon_0 \epsilon_r(x, y) \nabla \psi(x, y))|_{(x_i, y_j)} &\approx \epsilon_0 \frac{\epsilon_{r,i+\frac{1}{2},j} \left(\frac{\psi_{i+1,j} - \psi_{i,j}}{\Delta x_i} \right) - \epsilon_{r,i-\frac{1}{2},j} \left(\frac{\psi_{i,j} - \psi_{i-1,j}}{\Delta x_{i-1}} \right)}{\frac{1}{2}(\Delta x_i + \Delta x_{i-1})} \\ &+ \epsilon_0 \frac{\epsilon_{r,i,j+\frac{1}{2}} \left(\frac{\psi_{i,j+1} - \psi_{i,j}}{\Delta y_j} \right) - \epsilon_{r,i,j-\frac{1}{2}} \left(\frac{\psi_{i,j} - \psi_{i,j-1}}{\Delta y_{j-1}} \right)}{\frac{1}{2}(\Delta y_j + \Delta y_{j-1})} \end{aligned} \quad (3.24)$$

Here the relative permittivity ϵ is assumed to be linear between grid points and calculated by

$$\epsilon_{r,i\pm\frac{1}{2},j} = \frac{\epsilon_{r,i\pm 1,j} + \epsilon_{r,i,j}}{2} \quad \epsilon_{r,i,j\pm\frac{1}{2}} = \frac{\epsilon_{r,i,j\pm 1} + \epsilon_{r,i,j}}{2} \quad (3.25)$$

3 Numerical Methods

Inserting Eq.(3.24) into Eq. (3.13) results finally in the discretized poisson equation:

$$\begin{aligned} -\frac{\rho(x_i, y_i)}{\epsilon_0} &= \frac{\epsilon_{r,i+\frac{1}{2},j} \left(\frac{\psi_{i+1,j} - \psi_{i,j}}{\Delta x_i} \right) - \epsilon_{r,i-\frac{1}{2},j} \left(\frac{\psi_{i,j} - \psi_{i-1,j}}{\Delta x_{i-1}} \right)}{\frac{1}{2}(\Delta x_i + \Delta x_{i-1})} \\ &+ \frac{\epsilon_{r,i,j+\frac{1}{2}} \left(\frac{\psi_{i,j+1} - \psi_{i,j}}{\Delta y_j} \right) - \epsilon_{r,i,j-\frac{1}{2}} \left(\frac{\psi_{i,j} - \psi_{i,j-1}}{\Delta y_{j-1}} \right)}{\frac{1}{2}(\Delta y_j + \Delta y_{j-1})} \end{aligned} \quad (3.26)$$

Based on this equation it is possible to express $\psi_{i,j}$ by the potentials in the four neighboring grid points:

$$\psi_{i,j}(\psi_{i+1,j}, \psi_{i,j+1}, \psi_{i-1,j}, \psi_{i,j-1}) = \frac{1}{\alpha} [\beta + \gamma(\psi_{i+1,j}, \psi_{i,j+1}) + \delta(\psi_{i-1,j}, \psi_{i,j-1})] \quad (3.27)$$

with

$$\alpha = \frac{\epsilon_{r,i+\frac{1}{2},j}}{\Delta x_i} + \frac{\epsilon_{r,i-\frac{1}{2},j}}{\Delta x_{i-1}} + \frac{\epsilon_{r,i,j+\frac{1}{2}}}{\Delta y_j} + \frac{\epsilon_{r,i,j-\frac{1}{2}}}{\Delta y_{j-1}} \quad (3.28)$$

$$\beta = \frac{\rho_{i,j}}{\epsilon_0} \frac{(\Delta x_i + \Delta x_{i-1})}{2} \frac{(\Delta y_j + \Delta y_{j-1})}{2} \quad (3.29)$$

$$\gamma = \frac{\Delta y_j + \Delta y_{j-1}}{2} \left(\epsilon_{r,i+1,j} \frac{\psi_{i+1,j}}{\Delta x_i} \right) + \frac{\Delta x_i + \Delta x_{i-1}}{2} \left(\epsilon_{r,i,j+1} \frac{\psi_{i,j+1}}{\Delta y_j} \right) \quad (3.30)$$

$$\delta = \frac{\Delta x_i + \Delta x_{i-1}}{2} \left(\epsilon_{r,i,j-1} \frac{\psi_{i,j-1}}{\Delta y_{j-1}} \right) + \frac{\Delta y_j + \Delta y_{j-1}}{2} \left(\epsilon_{r,i-1,j} \frac{\psi_{i-1,j}}{\Delta x_{i-1}} \right) \quad (3.31)$$

for $i = 0, 1, \dots, N$ and $j = 0, 1, \dots, M$.

This system of linear equations must be solved for all $P_{i,j} \in \Omega$. As it can be seen easily this is impossible, since there are more $\psi_{i,j}$ than equations. To solve this problem boundary conditions must be implemented to reduce the number of unknown potentials. Then this system of linear equations can be solved iteratively in the domain Ω . For this purpose, an algorithm is proposed which is similar to the Gauß-Seidel method presented in section 3.1.

Beginning with the potential $\psi_{i,j}^0$, the $(k+1)$ -th step can be expressed by

$$\psi_{i,j}^{k+1}(\psi_{i+1,j}^k, \psi_{i,j+1}^k, \psi_{i-1,j}^{k+1}, \psi_{i,j-1}^{k+1}) = \frac{1}{\alpha} (\beta + \gamma(\psi_{i+1,j}^k, \psi_{i,j+1}^k) + \delta(\psi_{i-1,j}^{k+1}, \psi_{i,j-1}^{k+1})) \quad (3.32)$$

with the iteration index k and

$$\alpha = \frac{\epsilon_{r,i+\frac{1}{2},j}}{\Delta x_i} + \frac{\epsilon_{r,i-\frac{1}{2},j}}{\Delta x_{i-1}} + \frac{\epsilon_{r,i,j+\frac{1}{2}}}{\Delta y_j} + \frac{\epsilon_{r,i,j-\frac{1}{2}}}{\Delta y_{j-1}} \quad (3.33)$$

$$\beta = \frac{\rho_{i,j} (\Delta x_i + \Delta x_{i-1}) (\Delta y_j + \Delta y_{j-1})}{\epsilon_0 \cdot 2} \quad (3.34)$$

$$\gamma = \frac{\Delta y_j + \Delta y_{j-1}}{2} \left(\epsilon_{r,i+1,j} \frac{\psi_{i+1,j}}{\Delta x_i} \right) + \frac{\Delta x_i + \Delta x_{i-1}}{2} \left(\epsilon_{r,i,j+1} \frac{\psi_{i,j+1}}{\Delta y_j} \right) \quad (3.35)$$

$$\delta = \frac{\Delta x_i + \Delta x_{i-1}}{2} \left(\epsilon_{r,i,j-1} \frac{\psi_{i,j-1}}{\Delta y_{j-1}} \right) + \frac{\Delta y_j + \Delta y_{j-1}}{2} \left(\epsilon_{r,i-1,j} \frac{\psi_{i-1,j}}{\Delta x_{i-1}} \right) \quad (3.36)$$

The boundary conditions are chosen to satisfy the Neumann and Dirichlet conditions presented in Eq. (2.9) and Eq. (2.8). Fig. 3.2 shows an overview of the grid for a dual-gate OFET. For the potential at the boundaries to a metall (blue dots) the Dirichlet condition is used, while at the boundaries to vacuum (red dots) the potential must satisfy the Neumann condition (Eq. (2.9)).

Thus, the Dirichlet conditions (Eq. (2.8)) are given by

$$\begin{aligned} \bar{\psi}_{i,0} &= V_{GATE} && \text{for } 0 < i < M \\ \bar{\psi}_{i,N} &= V_{SUBSTRATE} && \text{for } 0 < i < M \\ \bar{\psi}_{i,j} &= V_{SOURCE} && \text{for } i \leq i_{SOURCE}, j_{OSC} < j < j_{ISOLATOR2} \\ \bar{\psi}_{i,j} &= V_{DRAIN} && \text{for } i \geq i_{DRAIN}, j_{OSC} < j < j_{ISOLATOR2} \end{aligned} \quad (3.37)$$

where $V_{GATE/SUBSTRATE/SOURCE/DRAIN}$ are the fixed potentials at the gate/substrate/source/drain. The indexes i_{SOURCE} and i_{DRAIN} are the grid points located at the boundaries of the source/drain contacts and j_{OSC} and $j_{ISOLATOR2}$ the indexes of the grid points located in the OSC/isolator next to source and drain.

The Neumann condition Eq. (2.9), in the case of the dual-gate OFET sketched in

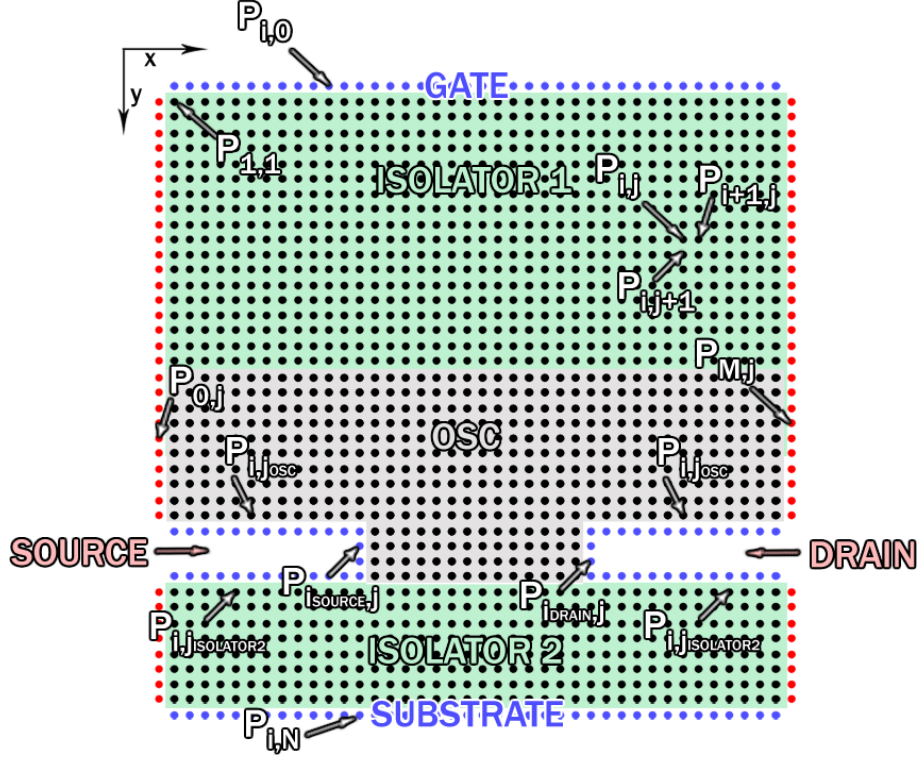


Figure 3.2: Boundary conditions for simulating a dual-gate OFET. The potential at the red dots needs to satisfy the Neumann condition, at the blue dots the Dirichlet condition and at the black dots the potential is calculated and initially chosen arbitrarily.

Fig. 3.2, reads

$$\left[\frac{\partial \psi(x, y)}{\partial x} \right]_{x=0} = 0 \quad (3.38)$$

$$\left[\frac{\partial \psi(x, y)}{\partial x} \right]_{x=x_M} = 0 \quad (3.39)$$

Using the finite difference approximation this results in

$$\left[\frac{\psi_{2,j} - \psi_{0,j}}{(\Delta x_0 + \Delta x_1)} \right] = 0 \quad \text{for } j = 1, \dots, j_{OSC}, j_{ISOLATOR 2}, \dots, N - 1$$

$$\left[\frac{\psi_{M,j} - \psi_{M-2,j}}{(\Delta x_{M-1} + \Delta x_{M-2})} \right] = 0 \quad \text{for } j = 1, \dots, j_{OSC}, j_{ISOLATOR 2}, \dots, N - 1$$
(3.40)

with the indexes j_{OSC} and $j_{ISOLATOR2}$ of the grid points located at the interface of the OSC/isolator to source and drain. As this equation must be maintained while doing the iteration, the relation between $\psi_{2,j}/\psi_{M,j}$ and $\psi_{0,j}/\psi_{M-2,j}$ is fulfilled by setting at each iteration step

$$\begin{aligned}\psi_{0,j}^{k+1} &= \psi_{2,j}^k & \text{for } j = 1, \dots, j_{OSC}, j_{ISOLATOR2}, \dots, N-1 \\ \psi_{M,j}^k &= \psi_{M-2,j}^{k+1} & \text{for } j = 1, \dots, j_{OSC}, j_{ISOLATOR2}, \dots, N-1\end{aligned}\quad (3.41)$$

with the iteration index k .

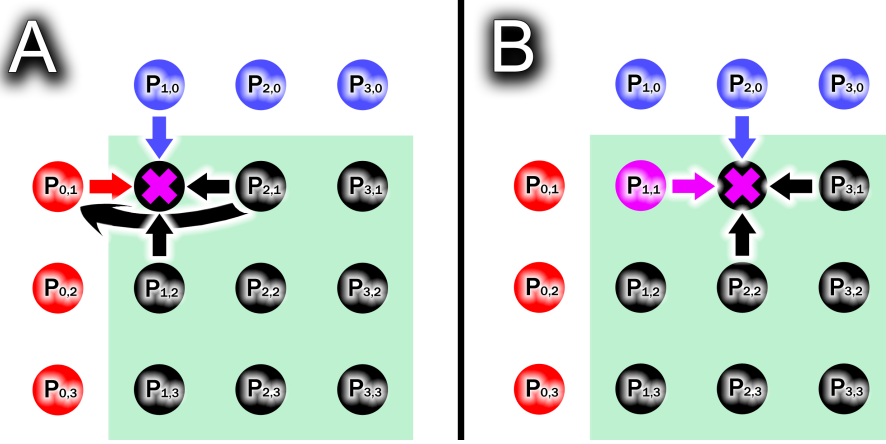


Figure 3.3: Beginning of the iterative calculation of the potential. Red dots indicate Neumann conditions, blue dots Dirichlet conditions. Violet x mark the grid points where the potential is calculated while the violet dot indicates a potential that has been calculated. In (A) the potential in the grid point $P_{1,1}$ only depends on the potential given in $P_{1,0}, P_{1,2}$ and $P_{2,1}$, because $\psi_{0,1} = \psi_{2,1}$. In (B) the potential in the next grid point $P_{2,1}$ is calculated with the use of $P_{1,1}$

As can be seen in Fig. 3.3 the iteration is started at $P_{1,1}$ and therefore the first potential calculated is $\psi_{1,1}^1(\psi_{2,1}^0, \psi_{1,2}^0, \psi_{0,1}^1, \psi_{1,0}^1)$. Using Eq. (3.32), Eq. (3.37) and Eq. (3.41) yields

$$\psi_{1,1}^1(\psi_{2,1}^0, \psi_{1,2}^0, \psi_{2,1}^0, V_{GATE}) \quad (3.42)$$

with $\psi_{1,2}^0$ and $\psi_{2,1}^0$ being arbitrarily chosen initial values and the constant V_{GATE} corresponding to the gate voltage applied. Now $\psi_{1,1}^1$ is used to calculate the potential $\psi_{2,1}^1$ at the next grid point:

$$\psi_{2,1}^1(\psi_{3,1}^0, \psi_{2,2}^0, \psi_{1,1}^1, V_{GATE}) \quad (3.43)$$

The solution is regarded convergent when the maximum error from one iteration step to the next is less than a predefined value η_P :

$$\Delta_{max}^k = |\psi_{i,j}^{k+1} - \psi_{i,j}^k|_{max} < \eta_P \quad (3.44)$$

3.4 Discretization of the current density and the continuity equation - the Scharfetter-Gummel algorithm

The current density equation (2.10) mentioned in section 2.1.3 can directly be inserted in the continuity equation (Eq. (2.13)). The resulting system of equations can be discretized by a simple finite differences method, but this approach is not recommended as it is very unstable. Therefore, a different approach has to be taken, as suggested by Scharfetter and Gummel [16].

Here, the current density equations are interpreted as a differential equations for $p(x, y)$ and $n(x, y)$, respectively, while assuming a constant current density $\mathbf{J}_{p/n}$ between two grid points. For one dimension this equation reads for the hole transport

$$J_{p,x} = qp(x)\mu_p E_x - D_p q \frac{\partial p(x)}{\partial x} = const, \quad \forall x \in [x_i, x_{i+1}] \quad (3.45)$$

The homogenous part is given by

$$0 = qp(x)\mu_p E_x - D_p q \frac{\partial p(x)}{\partial x}, \quad \forall x \in [x_i, x_{i+1}] \quad (3.46)$$

By using

$$a = q\mu_p E_x, \quad b = -qD_p, \quad (3.47)$$

this equation can be written as

$$0 = ap(x) + b \frac{\partial p(x)}{\partial x}, \quad \forall x \in [x_i, x_{i+1}] \quad (3.48)$$

Solved by an exponential ansatz $p = Ce^{\lambda x}$ this equation reads:

$$a \exp(\lambda x) + \lambda b \exp(\lambda x) = 0, \quad \forall x \in [x_i, x_{i+1}] \quad (3.49)$$

3 Numerical Methods

which leads to

$$p_{hom}(x) = C \exp\left(-\frac{a}{b}x\right), \quad \forall x \in [x_i, x_{i+1}] \quad (3.50)$$

Having found the homogeneous solution, the general solution can be obtained with the ansatz

$$p(x) = p_{hom}(x) + k, \quad \forall x \in [x_i, x_{i+1}] \quad (3.51)$$

Inserting Eq. (3.51) into Eq. (3.45) leads to

$$a(p_{hom}(x) + k) + b \frac{\partial p_{hom}(x)}{\partial x} = J_{p,x}, \quad \forall x \in [x_i, x_{i+1}] \quad (3.52)$$

and by using Eq. (3.50)

$$ak = J_{p,x} \rightarrow k = \frac{J_{p,x}}{a} \quad (3.53)$$

we obtain:

$$p(x) = C \exp\left(-\frac{a}{b}x\right) + \frac{J_{p,x}}{a}, \quad \forall x \in [x_i, x_{i+1}] \quad (3.54)$$

Reinserting Eq. (3.47) into Eq. (3.54) yields

$$p(x) = C \exp\left(\frac{\mu_p E_x}{D_p} x\right) + \frac{J_{p,x}}{q\mu_p E_x}, \quad \forall x \in [x_i, x_{i+1}] \quad (3.55)$$

Although Eq. (3.45) is a differential equation of first order, two boundary conditions are assumed, $p(x_i) = p_1$ and $p(x_i + \Delta x) = p_2$, which results in:

$$p_1 = C \exp\left(-\frac{a}{b}x_i\right) + \frac{J_{p,x}}{a} \quad (3.56)$$

$$p_2 = \left(p_1 - \frac{J_{p,x}}{a}\right) \exp\left(-\frac{a}{b}\Delta x\right) + \frac{J_{p,x}}{a} \quad (3.57)$$

This can be done because the current density $J_{p,x}$ is considered as an independent variable and an expression for $J_{p,x}$ can be found:

$$J_{p,x} = a \frac{p_2 - p_1 \exp\left(-\frac{a}{b}\Delta x\right)}{1 - \exp\left(-\frac{a}{b}\Delta x\right)} \quad (3.58)$$

This expression can be rewritten in the form

$$J_{p,x} = \frac{b}{\Delta x} \left[p_2 \frac{\Delta x \frac{a}{b}}{1 - \exp\left(-\frac{a}{b}\Delta x\right)} - p_1 \frac{-\Delta x \frac{a}{b}}{1 - \exp\left(+\frac{a}{b}\Delta x\right)} \right] \quad (3.59)$$

Inserting the Bernoulli function, defined by

$$B(x) = \frac{-x}{1 - \exp(x)} \quad (3.60)$$

leads to

$$J_{p,x} = \frac{b}{\Delta x} \left[p_2 B\left(-\frac{a}{b}\Delta x\right) - p_1 B\left(+\frac{a}{b}\Delta x\right) \right] \quad (3.61)$$

Using the Einstein relation (Eq. (2.12)) and taking the mean value of the diffusion constant between the neighboring grid points $D_{p,i+\frac{1}{2}}$, reinserting Eq. (3.47), replacing p_1 and p_2 by $p_{i,j}$ and $p_{i+1,j}$, $J_{p,x}$ by $J_{p,x,i+\frac{1}{2},j}$ and Δx by Δx_i leads to

$$J_{p,x,i+\frac{1}{2},j} = -\frac{qD_{p,i+\frac{1}{2},j}}{\Delta x_i} \left[p_{i+1,j} B\left(\frac{qE_x}{k_B T} \Delta x_i\right) - p_{i,j} B\left(-\frac{qE_x}{k_B T} \Delta x_i\right) \right] \quad (3.62)$$

with

$$D_{p,i+\frac{1}{2},j} = \frac{D_{p,i+1,j} + D_{p,i,j}}{2} \quad (3.63)$$

Using $E_x = -\frac{\psi_{i+1,j} - \psi_{i,j}}{\Delta x_i}$, we obtain

$$J_{p,x,i+\frac{1}{2},j} = -\frac{qD_{p,i+\frac{1}{2},j}}{\Delta x_i} \left[p_{i+1,j} B\left(-\frac{q(\psi_{i+1,j} - \psi_{i,j})}{k_B T}\right) - p_{i,j} B\left(+\frac{q(\psi_{i+1,j} - \psi_{i,j})}{k_B T}\right) \right] \quad (3.64)$$

The same procedure can be performed in y-direction and for negative charge carriers. The discretized drift-diffusion current for negative and positive charge carriers in x (index

i) and y (index j) direction at time t are then given by

$$\begin{aligned}
 J_{p,x,i+\frac{1}{2},j}^t &= -\frac{qD_{p,i+\frac{1}{2},j}}{\Delta x_i} \left[p_{i+1,j}^t B\left(-\frac{q(\psi_{i+1,j}^t - \psi_{i,j}^t)}{k_B T}\right) - p_{i,j}^t B\left(\frac{q(\psi_{i+1,j}^t - \psi_{i,j}^t)}{k_B T}\right) \right] \\
 J_{p,y,i,j+\frac{1}{2}}^t &= -\frac{qD_{p,i,j+\frac{1}{2}}}{\Delta y_j} \left[p_{i,j+1}^t B\left(-\frac{q(\psi_{i,j+1}^t - \psi_{i,j}^t)}{k_B T}\right) - p_{i,j}^t B\left(\frac{q(\psi_{i,j+1}^t - \psi_{i,j}^t)}{k_B T}\right) \right] \\
 J_{n,x,i+\frac{1}{2},j}^t &= \frac{qD_{n,i+\frac{1}{2},j}}{\Delta x_i} \left[n_{i+1,j}^t B\left(\frac{q(\psi_{i+1,j}^t - \psi_{i,j}^t)}{k_B T}\right) - n_{i,j}^t B\left(-\frac{q(\psi_{i+1,j}^t - \psi_{i,j}^t)}{k_B T}\right) \right] \\
 J_{n,y,i,j+\frac{1}{2}}^t &= \frac{qD_{n,i,j+\frac{1}{2}}}{\Delta y_j} \left[n_{i,j+1}^t B\left(\frac{q(\psi_{i,j+1}^t - \psi_{i,j}^t)}{k_B T}\right) - n_{i,j}^t B\left(-\frac{q(\psi_{i,j+1}^t - \psi_{i,j}^t)}{k_B T}\right) \right]
 \end{aligned} \tag{3.65}$$

The continuity equation Eq (2.13) for the hole current density \mathbf{J}_p is given by

$$\frac{1}{q} \nabla \cdot \mathbf{J}_p + \frac{\partial p}{\partial t} = G \tag{3.66}$$

By using the finite differences method for the approximation of the divergence of a vector field (Eq. 3.21) and the implicit Euler backward method for the time dependency (Eq (3.12)) we obtain

$$\frac{1}{q} \frac{J_{p,x,i+\frac{1}{2},j}^{t+\Delta t} - J_{p,x,i-\frac{1}{2},j}^{t+\Delta t}}{\frac{1}{2}(\Delta x_i + \Delta x_{i-1})} + \frac{1}{q} \frac{J_{p,y,i,j+\frac{1}{2}}^{t+\Delta t} - J_{p,y,i,j-\frac{1}{2}}^{t+\Delta t}}{\frac{1}{2}(\Delta y_j + \Delta y_{j-1})} + \frac{p_{i,j}^{t+\Delta t} - p_{i,j}^t}{\Delta t} = G_{i,j}^{t+\Delta t} \tag{3.67}$$

As mentioned in section 3.2 the great advantage of using an implicit method is the stability and the possibility of performing larger time steps and, therefore, a faster convergence to the steady state.

Combining Eq. (3.65) and Eq. (3.67) leads to

$$\begin{aligned}
 & \frac{1}{\frac{1}{2}q(\Delta x_i + \Delta x_{i-1})} \\
 & \times \left\{ -q \frac{D_{p,i+\frac{1}{2},j}}{\Delta x_i} \left[p_{i+1,j}^{t+\Delta t} B\left(-\frac{q(\psi_{i+1,j}^{t+\Delta t} - \psi_{i,j}^{t+\Delta t})}{k_B T}\right) - p_{i,j}^{t+\Delta t} B\left(\frac{q(\psi_{i+1,j}^{t+\Delta t} - \psi_{i,j}^{t+\Delta t})}{k_B T}\right) \right] \right. \\
 & \quad \left. + q \frac{D_{p,i-\frac{1}{2},j}}{\Delta x_{i-1}} \left[p_{i,j}^{t+\Delta t} B\left(-\frac{q(\psi_{i,j}^{t+\Delta t} - \psi_{i-1,j}^{t+\Delta t})}{k_B T}\right) - p_{i-1,j}^{t+\Delta t} B\left(\frac{q(\psi_{i,j}^{t+\Delta t} - \psi_{i-1,j}^{t+\Delta t})}{k_B T}\right) \right] \right\} \\
 & + \frac{1}{\frac{1}{2}q(\Delta y_j + \Delta y_{j-1})} \\
 & \times \left\{ -q \frac{D_{p,i,j+\frac{1}{2}}}{\Delta y_j} \left[p_{i,j+1}^{t+\Delta t} B\left(-\frac{q(\psi_{i,j+1}^{t+\Delta t} - \psi_{i,j}^{t+\Delta t})}{k_B T}\right) - p_{i,j}^{t+\Delta t} B\left(\frac{q(\psi_{i,j+1}^{t+\Delta t} - \psi_{i,j}^{t+\Delta t})}{k_B T}\right) \right] \right. \\
 & \quad \left. + q \frac{D_{p,i,j-\frac{1}{2}}}{\Delta y_{j-1}} \left[p_{i,j}^{t+\Delta t} B\left(-\frac{q(\psi_{i,j}^{t+\Delta t} - \psi_{i,j-1}^{t+\Delta t})}{k_B T}\right) - p_{i,j-1}^{t+\Delta t} B\left(\frac{q(\psi_{i,j}^{t+\Delta t} - \psi_{i,j-1}^{t+\Delta t})}{k_B T}\right) \right] \right\} \\
 & + \frac{p_{i,j}^{t+\Delta t} - p_{i,j}^t}{\Delta t} = G_{i,j}^{t+\Delta t} \tag{3.68}
 \end{aligned}$$

Expressing $p_{i,j}^{t+\Delta t}$ as a function of the hole density at its four neighboring grid points and $p_{i,j}^t$ leads to

$$p_{i,j}^{t+\Delta t}(p_{i,j}^t, p_{i,j-1}^{t+\Delta t}, p_{i-1,j}^{t+\Delta t}, p_{i+1,j}^{t+\Delta t}, p_{i,j+1}^{t+\Delta t}) = \frac{1}{\alpha} [\beta(p_{i,j}^t) + \gamma(p_{i,j-1}^{t+\Delta t}, p_{i-1,j}^{t+\Delta t}) + \delta(p_{i+1,j}^{t+\Delta t}, p_{i,j+1}^{t+\Delta t})] \tag{3.69}$$

with

$$\begin{aligned}
 \alpha &= D_{n,i,j-\frac{1}{2}} B \left(\frac{\psi_{p,i,j-1}^{t+\Delta t} - \psi_{p,i,j}^{t+\Delta t}}{V_T} \right) \frac{\Delta x_{i-1} + \Delta x_i}{2\Delta y_{j-1}} \\
 &+ D_{p,i-\frac{1}{2},j} B \left(\frac{\psi_{p,i-1,j}^{t+\Delta t} - \psi_{p,i,j}^{t+\Delta t}}{V_T} \right) \frac{\Delta y_{j-1} + \Delta y_j}{2\Delta x_{i-1}} \\
 &+ D_{p,i+\frac{1}{2},j} B \left(\frac{\psi_{p,i+1,j}^{t+\Delta t} - \psi_{p,i,j}^{t+\Delta t}}{V_T} \right) \frac{\Delta y_{j-1} + \Delta y_j}{2\Delta x_{i-1}} \\
 &+ D_{p,i,j+\frac{1}{2}} B \left(\frac{\psi_{p,i,j+1}^{t+\Delta t} - \psi_{p,i,j}^{t+\Delta t}}{V_T} \right) \frac{\Delta x_{i-1} + \Delta x_i}{2\Delta y_{j-1}} \\
 &+ \frac{1}{\Delta t} \frac{\Delta x_{i-1} + \Delta x_i}{2} \frac{\Delta y_{j-1} + \Delta y_j}{2} \\
 \beta &= \left(G_{i,j}^{t+\Delta t} + \frac{p_{i,j}^t}{\Delta t} \right) \frac{\Delta x_{i-1} + \Delta x_i}{2} \frac{\Delta y_{j-1} + \Delta y_j}{2} \\
 \gamma &= p_{i,j-1}^{t+\Delta t} D_{p,i,j-\frac{1}{2}} B \left(\frac{\psi_{p,i,j}^{t+\Delta t} - \psi_{p,i,j-1}^{t+\Delta t}}{V_T} \right) \frac{\Delta x_{i-1} + \Delta x_i}{2\Delta y_{j-1}} \\
 &+ p_{i-1,j}^{t+\Delta t} D_{p,i-\frac{1}{2},j} B \left(\frac{\psi_{p,i,j}^{t+\Delta t} - \psi_{p,i-1,j}^{t+\Delta t}}{V_T} \right) \frac{\Delta y_{j-1} + \Delta y_j}{2\Delta x_{i-1}} \\
 \delta &= p_{i+1,j}^{t+\Delta t} D_{p,i+\frac{1}{2},j} B \left(\frac{\psi_{p,i+1,j}^{t+\Delta t} - \psi_{p,i,j}^{t+\Delta t}}{V_T} \right) \frac{\Delta y_{j-1} + \Delta y_j}{2\Delta x_{i-1}} \\
 &+ p_{i,j+1}^{t+\Delta t} D_{p,i,j+\frac{1}{2}} B \left(\frac{\psi_{p,i,j+1}^{t+\Delta t} - \psi_{p,i,j}^{t+\Delta t}}{V_T} \right) \frac{\Delta x_{i-1} + \Delta x_i}{2\Delta y_{j-1}} \tag{3.70}
 \end{aligned}$$

For negative charge carriers a similar expression can be found, but as mentioned in section 2.2 only positive charge transport is assumed and negative charge transport neglected.

This coupled system of $N \times M$ linear equations must now be solved. Similar to the Gauß-Seidel method (Eq. (3.1)) and the proposed method for solving the Poisson equation (Eq. (3.32)-Eq. (3.36)) this is done iteratively:

$$p_{i,j}^{t+\Delta t} (p_{i,j}^t, p_{i,j-1}^{t+\Delta t}, p_{i-1,j}^{t+\Delta t}, p_{i+1,j}^{t+\Delta t}, p_{i,j+1}^{t+\Delta t}) \rightarrow p_{i,j}^{t+\Delta t,k+1} (p_{i,j}^{t,k}, p_{i,j-1}^{t+\Delta t,k+1}, p_{i-1,j}^{t+\Delta t,k+1}, p_{i+1,j}^{t+\Delta t,k}, p_{i,j+1}^{t+\Delta t,k}) \tag{3.71}$$

with the iteration index k until a certain exit condition with a predefined limit η_D is

met:

$$|p_{i,j}^{t+\Delta t,k+1} - p_{i,j}^{t+\Delta t,k}| \leq \eta_D \quad (3.72)$$

Because charge carrier transport is only possible in the OSC, this system of equations just needs to be solved for the area S_{OSC} with

$$S_{OSC} = \{P_{i,j} | 0 < i < M \text{ for } j_{ISOLATOR1} < j \leq j_{OSC}, \\ i_{SOURCE} < i < i_{DRAIN} \text{ for } j_{OSC} < j < j_{ISOLATOR2}\} \quad (3.73)$$

S_{OSC} and its boundary conditions are shown in Fig. 3.4

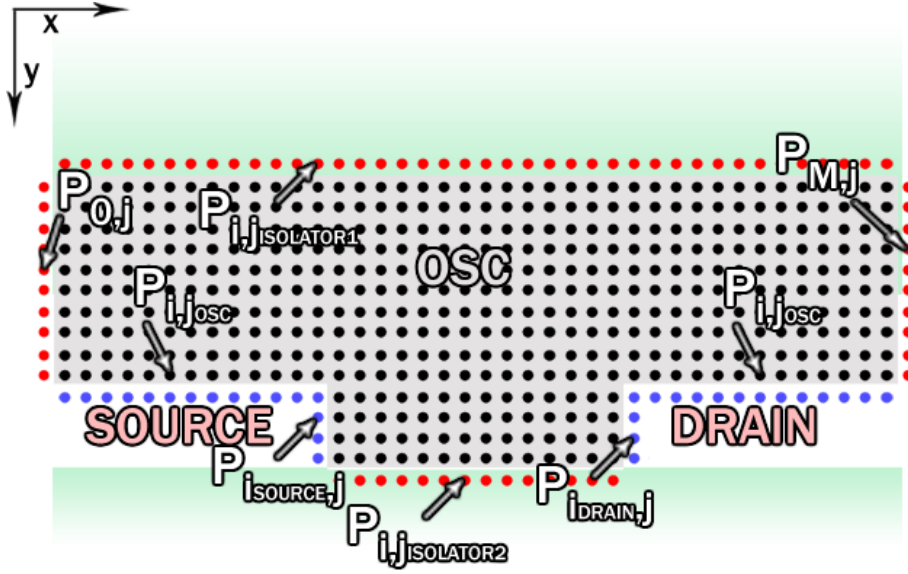


Figure 3.4: Boundary conditions for simulating a dual-gate OFET. At the red dots the Neumann condition is applied while at the blue dots the Dirichlet condition is used.

The Dirichlet condition is realized by

$$p_{i,j}^{t,k} = p_{constant} \begin{cases} \text{for } i \leq i_{SOURCE}, j_{OSC} < j < j_{ISOLATOR2} \\ \text{for } i \geq i_{DRAIN}, j_{OSC} < j < j_{ISOLATOR2} \end{cases} \quad (3.74)$$

for $t \geq 0$ and $k \geq 0$, where $p_{constant}$ is calculated by using Eq. (2.17).

The Neumann condition is satisfied by

$$\begin{aligned}
 p_{0,j}^{t,k+1} &= p_{2,j}^{t,k} && \text{for } j_{ISOLATOR1} < j \leq j_{OSC} \\
 p_{N,j}^{t,k+1} &= p_{N-2,j}^{t,k+1} && \text{for } j_{ISOLATOR1} < j \leq j_{OSC} \\
 p_{i,j_{ISOLATOR1}}^{t,k+1} &= p_{i,j_{ISOLATOR1}+2}^{t,k} && \text{for } 0 < i < M \\
 p_{i,j_{ISOLATOR2}}^{t,k+1} &= p_{i,j_{ISOLATOR2}-2}^{t,k+1} && \text{for } i_{SOURCE} < i < i_{DRAIN}
 \end{aligned} \tag{3.75}$$

for all $t \geq 0$ and $k \geq 0$.

The iteration process itself is similar to that of the Poisson equation described by Eq. (3.42) - Eq. (3.43), but instead of beginning in $P_{1,1}$ it is now started in $P_{1,j_{ISOLATOR1}+1}$ (see also Fig. 3.3).

3.5 The Algorithm of the simulation

The main goal of this thesis is to calculate the current dependent on the applied potentials at source, drain and gate. To achieve this, the Poisson equation and the continuity equation are solved self-consistently. At a given time t this is done by solving first the Poisson equation, then calculating the mobility depending on the hole density. The potential and the hole density are used in the drift diffusion model for solving the continuity equation. The result are new hole densities, which are used to calculate the new potential at a time $t + \Delta t$. This is repeated until a steady state is reached. In Fig 3.5 an overview of the used algorithm is presented.

The exit condition for the steady state is given by

$$\begin{aligned}
 \delta_1 &> \frac{I_{max} - I_{min}}{I_{min}} \\
 \delta_2 &> \Delta p_{\Delta t, max}
 \end{aligned} \tag{3.76}$$

where δ_1 and δ_2 are predefined values and $\Delta p_{\Delta t, max}$ the maximum change of the charge carrier density during one time interval Δt . Further, $I_{max/min}$ are the maximum/minimum of the current in every cross-section in y-direction between source and drain.

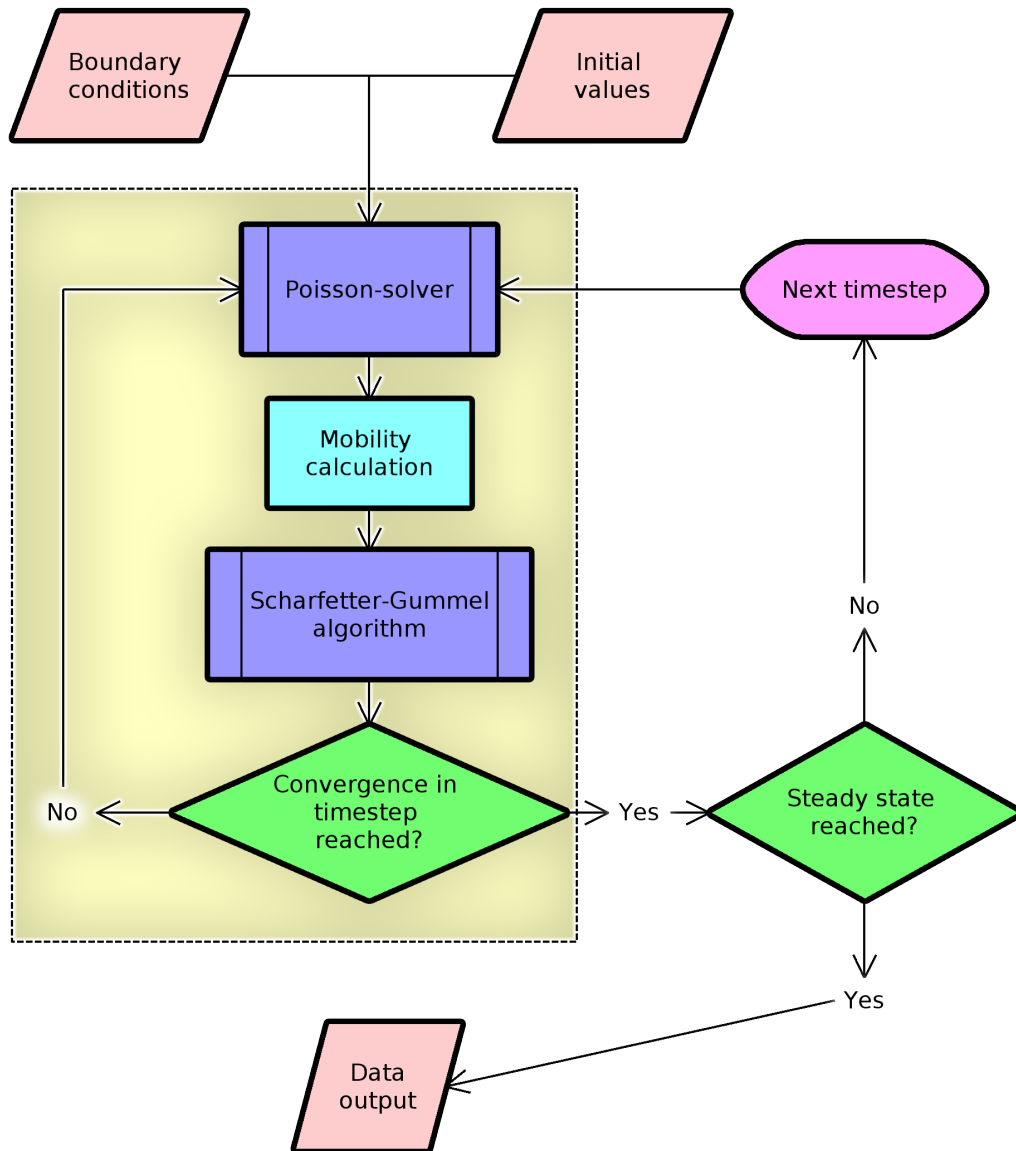


Figure 3.5: Flowchart of the algorithm

4 Results

This chapter is divided into two parts: The first section summarizes the experimental results with particular focus on the change of the current in the presence of ammonia. The second part is dedicated to the simulation results. Before actually comparing the results of the simulation with the experimental data, the influence of some important parameters is studied, i.e. the height of the injection barrier, the mobility, different dielectric constants, and the influence of the substrate potential. Then, by using a certain justified set of parameters, the I-V curves of the device without the presence of ammonia are computed. Based on these parameters three different scenarios are tested: a change in the dielectric constant, presence of immobile charges, and accumulation of mobile charges at the PVA-P3HT interface. These scenarios are then compared to the experimental data.

4.1 Experimental results

The device examined in this thesis is a dual-gate OFET (section 2.2.2) with a ROM-polymer (section 2.3) as one of the two isolating materials. First built by Andreas Klug et al. [2], the idea of this OFET was to build an ammonia sensitive device. The complete design is shown in Fig. 4.1.

To monitor the impact of the NH_3 , the potential at the source (V_S) and the drain contact (V_D) were set to fixed values, while the potential at the gate (V_G) was varied. While V_S was set to 0 for all measurements, transfer characteristics were measured for $V_D = -25\text{V}$, $V_D = -45\text{V}$ and $V_D = -85\text{V}$ before and after exposition to ammonia. These are shown in Fig. 4.2 as well as a common diagram of all characteristics (Fig. 4.3) for a better comparison.

As easily can be seen, there is an increase by an order of magnitude in the current due to the presence of ammonia, e.g. for $V_G = -85\text{V}$ the current increases by more than 800%. Also a change in the threshold voltage V_{th} can be observed. Especially the logarithmic plot of the characteristics in Fig. 4.3 shows that no threshold voltage can be seen in the

4 Results

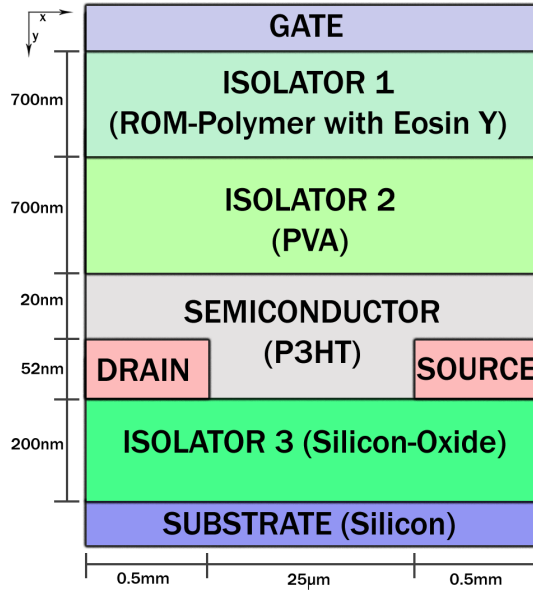


Figure 4.1: A sketch of the complete design of the device examined.

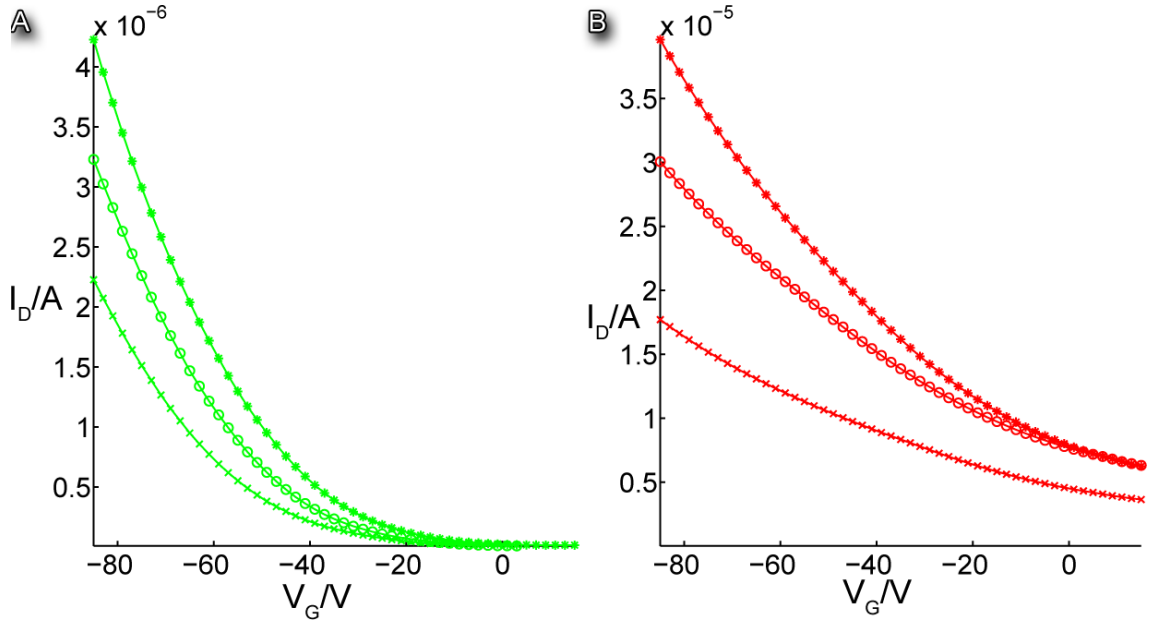


Figure 4.2: Transfer characteristics (A) with and (B) without the presence of ammonia at three different drain potentials V_D ($V_D = -25\text{V}$ (cross), -45V (circle), -85V (star)).

characteristics with the presence of ammonia, while $V_{th} = 0\text{V}$ without the presence of ammonia.

Plausible explanations of the effect include, but are not limited to, the following three

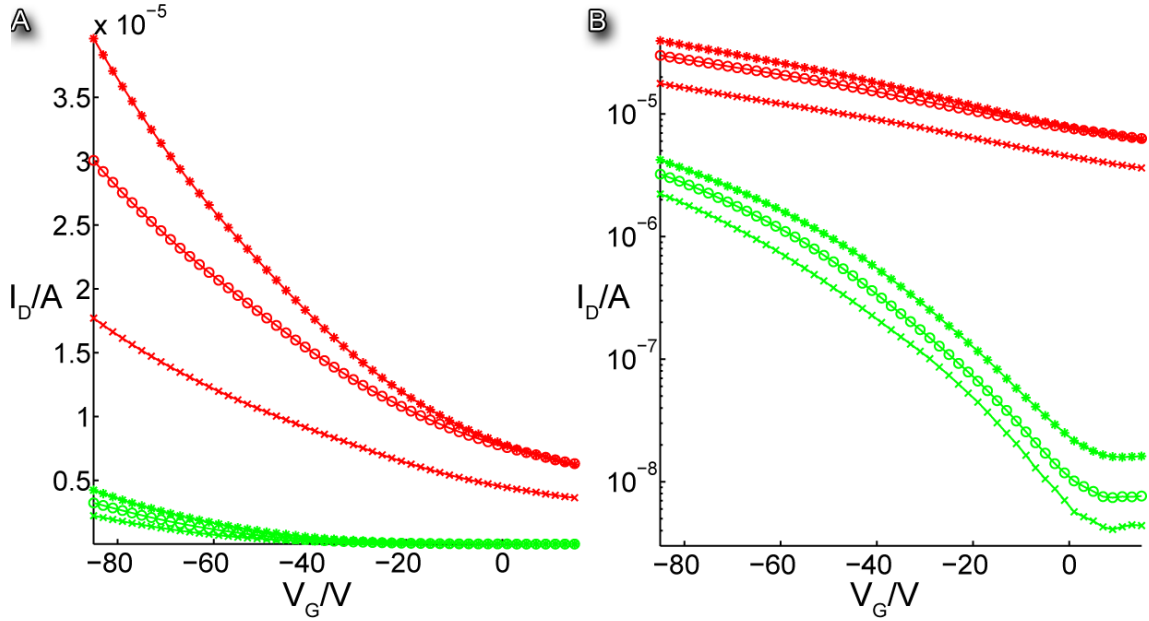


Figure 4.3: Comparison of the transfer characteristics with (red) and without (green) the presence of ammonia at the same three different drain potentials $V_D = -25\text{V}$ (cross), -45V (circle), -85V (star) in a (A) linear and (B) logarithmic plot

assumptions:

- Change in the dielectric constant (ϵ_r): Measurements of the dielectric constant without and with the presence of ammonia showed an increase from $\epsilon_r = 6.0$ to $\epsilon_r = 6.5$ [2]. A change in the dielectric constant results in an increase of the capacitance of the the device. This results in a higher current as can be seen from Eq. (2.18) and Eq. (2.19) and has been exploited in electrolyte-gated OFETs demonstrated, e.g., by Panzer et al. [22].
- Immobile charges: As mentioned in section 2.3, the ammonia reacts with the Eosin-Y groups of the ROM-polymer. This results in a positively charged ammonium molecule and a negatively charged O^- -group. While the ammonium ions migrate to the gate, where they are supposed to become neutral or dissolve, the negative charges remain fixed in space and produce a space charge layer. This would also change the capacitance of the polymer and, thus, the current. Additionally, a threshold voltage shift can be expected [18].
- Mobile charges: Also mentioned in section 2.3 is the possibility of negative mobile charges. These accumulate at the PVA-P3HT interface and generate there a surface charge layer. This surface charge layer influences the capacitance, the current,

and the threshold voltage [18].

As these potential explanations can hardly be discriminated by experimental measurements, they are incorporated in the simulation model described in chapter 3. The simulation validates one of the scenarios given above if (a) the associated parameters chosen reproduce the transfer characteristic of the pristine device, (b) the increase in the current is observed, and (c) the threshold voltage is located beyond the interval $-85\text{V} < V_G < 15\text{V}$ upon exposure to ammonia.

Beside the three contact potentials V_S , V_D , and V_G , the potential at the substrate (V_{SUBS}) is an important factor for the characteristics of the device. Albeit its importance, no data regarding this parameter has been experimentally acquired so far. Therefore, it remains unclear, whether the substrate was set to ground or was left floating; it could have adopted any arbitrary value [2]. This problem is discussed in more detail in section 4.2.1.

4.2 Simulation studies

Although the goal of any simulation is to approximate the real circumstances as closely as possible, the computational effort necessitates further simplification in addition to the ones mentioned in chapter 3. As seen in Fig. 4.1, the length of the contacts is 20 times larger than the length of the channel. Assuming that the main activity of the device takes place between source and drain, it is possible to relocate the boundaries and reduce the length of the contacts to $5\mu\text{m}$. This reduction is shown in Fig. 4.4. With the smaller device, the computational effort is reduced and the algorithm discussed in chapter 3 is used for simulating the device.

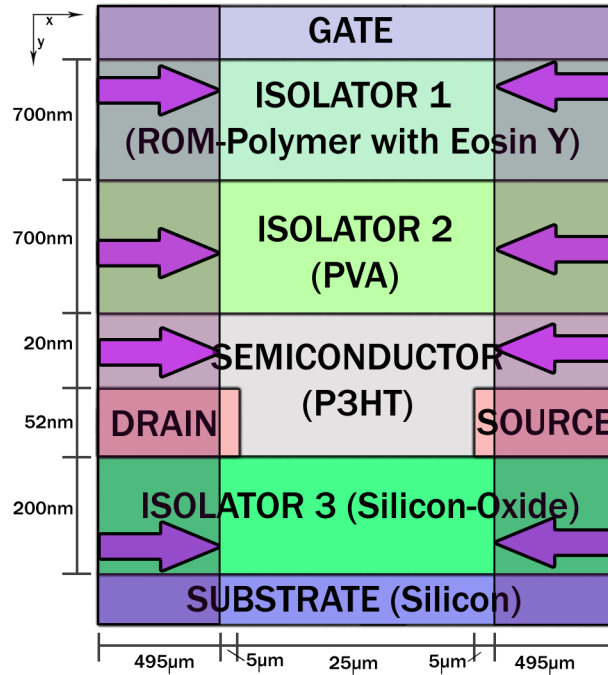


Figure 4.4: Reduction of the length of the device by relocating the boundaries to reduce computational effort.

In the first part of this section, the influence of the most important transport parameters is investigated to gain insight into the dependencies of the transfer characteristic for this device layout. These parameters are the dielectric constant ϵ_r , the mobility μ , the height of the injection barrier Δ_b , and the substrate potential V_{SUBS} .

In the second part, a fixed set of parameters that is justified for the materials used, is employed to simulate the characteristics of the device without ammonia. Then, the response to ammonia exposure is simulated by three different setups: First solely by a change in the dielectric constant, second by a change in the dielectric constant and an

additional constant charge density in the ROM-polymer, and third by a change in the dielectric constant and a surface charge layer located at the interface between P3HT and PVA.

4.2.1 Parameter studies

In this subsection the influence of some of the most important parameters of the device (see section 4.1) on the transfer characteristic is investigated. To accomplish this a set of parameter is used, whose values are typical for the considered materials. These values are given in Tab. 4.1. The potentials at the substrate and the source are set

Table 4.1: Set of parameters used for parameter studies

μ_0	0.4×10^{-6}	$\frac{m^2}{Vs}$
ϵ_{SiO_x}	4.5	
ϵ_{OSC}	3.2	
ϵ_{PVA}	8.4	
$\epsilon_{ROM-polymer}$	6	
T	298.15	K
N_{HOMO}	2×10^{27}	$\frac{1}{m^3}$
Δ_h	0.1	eV

to $V_{SUBS} = V_S = 0V$, the potential at the drain V_D is set to $-25V$, $-45V$ and $-85V$, respectively. The results can be seen in Fig. 4.5. It is clear from the comparison to the experimental curves that the parameters used overestimate the slope of the I-V curves. Additionally, the offset between the three simulated curves related to different V_D does not nearly reproduce the experiment as the three simulated characteristics are hardly different. In a three-dimensional plot of the potential distribution it can be seen, why the influence of V_D is much less pronounced than expected for a prototypical single-gate OFET. In Fig. 4.6, the initial (C) and the steady state (D) potential distribution of the device for $V_G = -85V$ is shown in comparison to the corresponding quantities (A,B) for

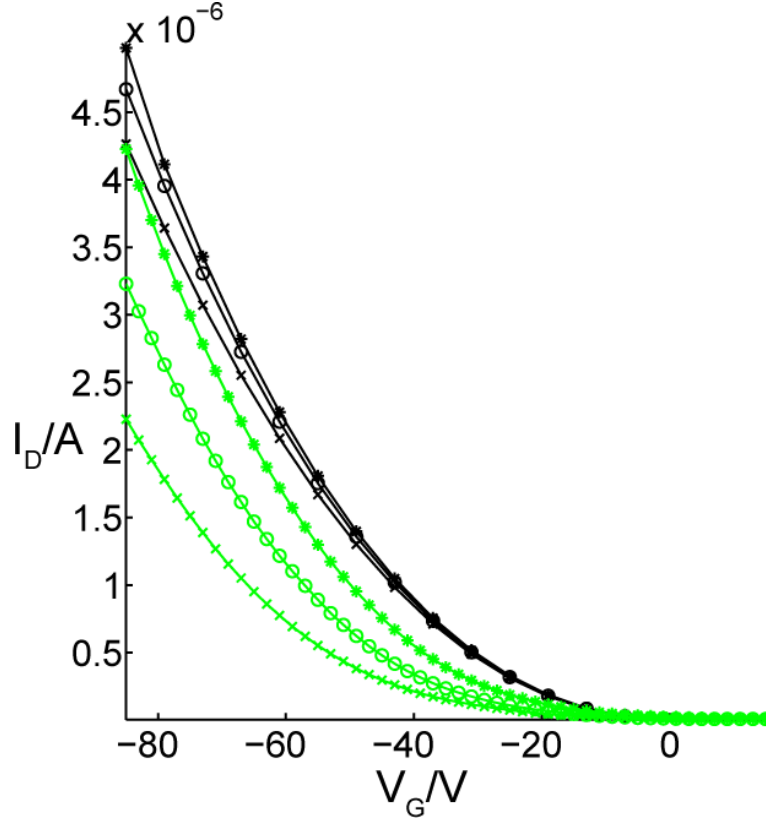


Figure 4.5: Simulation (black) of the device with $V_{SUBS} = 0V$ at $V_D = -25V$ (cross), $V_D = -45V$ (circles) and $V_D = -85V$ (stars) compared to the experimental results (green).

a single-gate device of the same layout apart from replacing the $\text{SiO}_x\text{-Si}$ substrate with vacuum, i.e., by setting $\epsilon_{\text{SiO}_x} = \epsilon_{SUBS} = 1$.

A closer inspection of the initial potential evolution reveals pronounced differences in the OSC region (A,C). In the case of the single-gate OFET (A), the potential adopts the gate value except in the regions covered by the source and drain contacts [18]. In (C), on the other hand, the potential in the OSC is mainly influenced by the substrate, rather than by the gate. This is because the distance between OSC and gate is seven times larger (1400nm) than the distance between OSC and substrate (200nm). Also, in (C), an electric field can be observed in the OSC in y -direction. The source-drain bias has a markedly small influence on the potential distribution in the OSC in both devices (A,C) due to a contact separation of $25\mu m$.

From the comparison of the steady-state potentials (B,D) it becomes evident that the influence of the source-drain bias on the channel is significantly reduced due to the presence of a second gate (D). In the single-gate OFET (B), the corresponding electric

4 Results

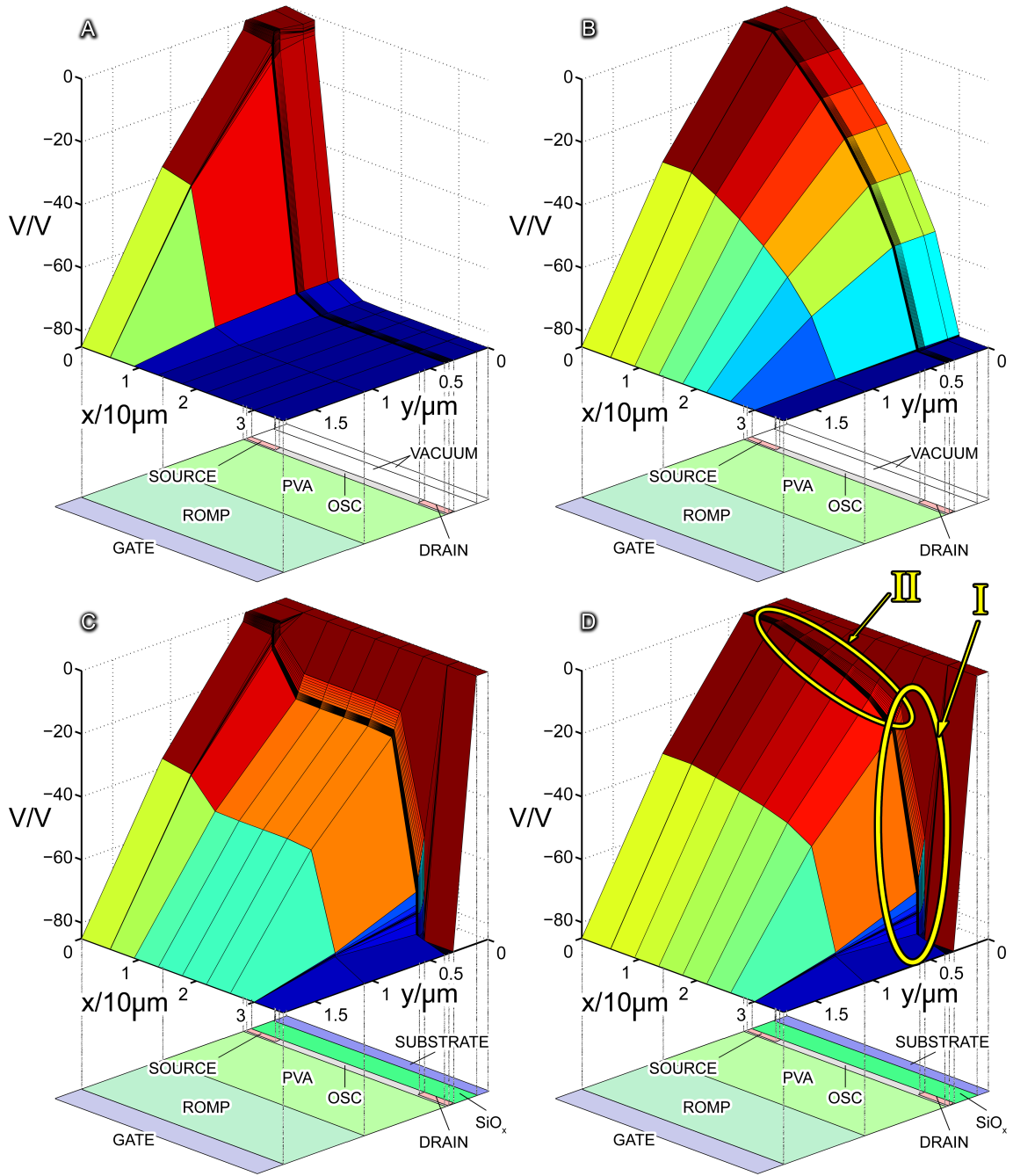


Figure 4.6: Potential distribution for (A) the initial and (B) the steady state of a single-gate OFET (see text) and (C) the initial and (D) the steady state for the dual-gate device for $V_{SUBS} = 0V$, $V_D = -85V$, $V_G = -85V$. Arrow I depicts the high electric field next to the drain contact, arrow II the region of a low electric field in most of the channel.

field along the channel increases continuously, while in (D) the electric field in most of

the channel is more or less constant (see arrow II) due to the substrate located very near to the channel (200 nm). Solely near the drain electrode (see arrow I) the electric field increases drastically. Therefore, the offset of the three transfer curves with respect to V_D is much smaller than in a single-gate OFET.

In the following, selected parameters will be varied in order to study their impact on the shape of the I-V curves and to judge whether a suggested sensing scenario is reasonable.

Change in the dielectric constant $\epsilon_{ROM-polymer}$: As said before in subsection 4.1, the dielectric constant of the ROM-polymer changes in the presence of ammonia. Measurements showed an increase of 0.5, shifting the $\epsilon_{ROM-polymer}$ from 6.0 to 6.5 [2]. To study the influence of this change on the transfer characteristic, a simulation is done by using the set of parameters presented in Tab. 4.1 with an altered dielectric constant for the ROM-polymer $\epsilon_{ROM-polymer} = 6.5$. For a better comparison the results are plotted in a common plot with the former results (Fig. 4.7). Although a slight increase of the

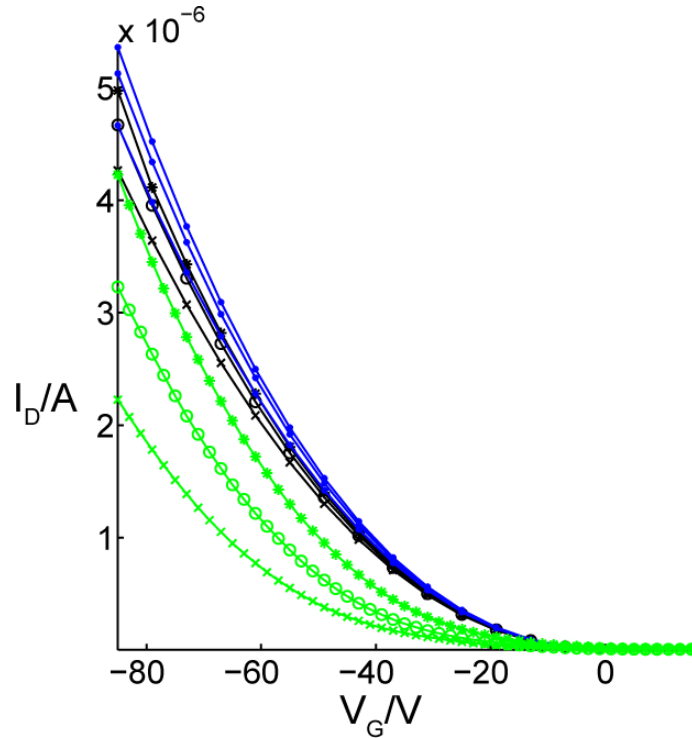


Figure 4.7: Simulation of the increase of the dielectric constant ϵ_r from 6.0 (black) to 6.5 (blue). This is done for three different drain potentials $V_D = -25V$ (cross), $V_D = -45V$ (circles) and $V_D = -85V$ (stars) and compared to the experimental results without the presence of ammonia (green).

current is observed, the influence of this change is lower than 10%. Additionally, no change in the threshold voltage is observed. Thus, such a shift in the dielectric constant cannot solely explain the effects seen in the measurements (see subsection 4.1).

Change in the mobility μ_0 : One of the most important parameters describing the charge carrier transport is the mobility. It is discussed in subsection 2.1.1 and incorporated in the simulation model by Eq. (2.1). With testing the influence of μ_0 on the transfer characteristic, it can be determined, whether the exposure with NH_3 is profoundly altering the carrier mobility. The same set of parameters is used as presented in Tab. 4.1 with exception of the mobility. In Fig. 4.8 the results of the simulation with $\mu_0 = 0.4 \times 10^{-5} \frac{\text{m}^2}{\text{Vs}}$ (blue) and $\mu_0 = 0.4 \times 10^{-6} \frac{\text{m}^2}{\text{Vs}}$ (green) are shown, as well as the experimental results with and without ammonia.

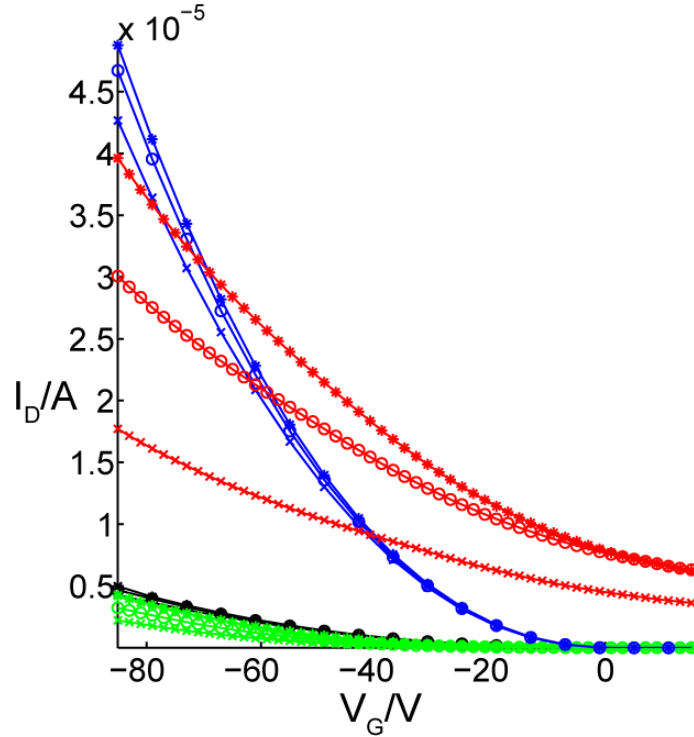


Figure 4.8: Simulation of the increase of the mobility μ_0 from $\mu_0 = 0.4 \times 10^{-6} \frac{\text{m}^2}{\text{Vs}}$ (black) to $\mu_0 = 0.4 \times 10^{-5} \frac{\text{m}^2}{\text{Vs}}$ (blue). This is done for three different drain potentials $V_D = -25\text{V}$ (cross), $V_D = -45\text{V}$ (circles) and $V_D = -85\text{V}$ (stars) and compared to the experimental results without (green) and with (red) the presence of ammonia.

By increasing the mobility by a factor 10, the current increases by more than 1000% at $V_G = -85\text{V}$. This is not surprising, as the current density is directly proportional

to the mobility according to the current density equations (Eq. 2.10) with the Einstein relation (Eq. 2.12). Additionally, it can be seen that, although the offset between the three simulated curves increases with higher mobility, it is still smaller than the experimentally measured ones. Note, however, that the threshold voltage does not change and remains at $V_{th} = 0V$. Thus, a μ enhancement due to NH_3 exposure can be ruled out as primary origin of the current increase.

Change in the injection barrier (Δ_h): Another important parameter is the height of the injection barrier, intensively discussed in subsection 2.17. This barrier could be possibly altered in the course of operation in the presence of ammonia. Again using the set of parameters introduced at the beginning of this subsection in Tab. 4.1, the injection barrier is chosen to be $\Delta_h = 0.1eV$ and $\Delta_h = 1eV$. The results of the simulations is shown in Fig. 4.9, where they are plotted together with the experimental results without ammonia. Although the injection barrier is increased by a factor 10, the transfer

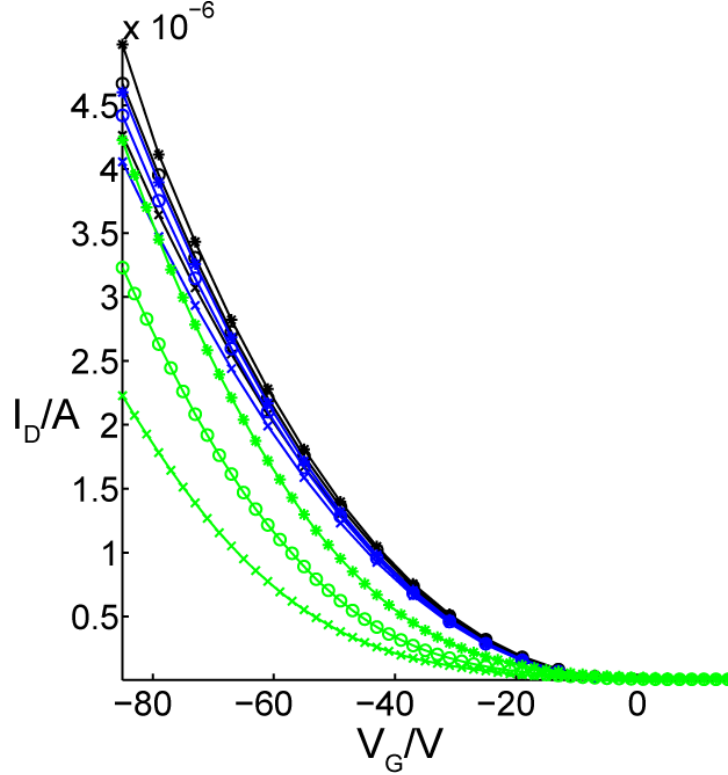


Figure 4.9: Simulation of the change in the injection barrier Δ_h from $\Delta_h = 0.1eV$ (black) to $\Delta_h = 1eV$ (blue). This is done for three different drain potentials $V_D = -25V$ (cross), $V_D = -45V$ (circles) and $V_D = -85V$ (stars) and compared to the experimental results without the presence of ammonia (green).

characteristics hardly change. Modifications of the injection barrier seem to have little influence in the characteristics, and, thus, cannot be responsible of the sensing effect.

Influence of the substrate potential: The substrate is made of highly doped silicone with a specific resistance of 3-5 Ω . Therefore, it is treated in this thesis as a conducting material. As mentioned in section 4.1 the actual potential at the substrate is not known. Thus, one needs to anticipate throughout the simulations that its potential could have adopted an arbitrary value during the measurement. If the substrate has no connection to another conductive material, its potential can only be influenced by the gate, drain, and source potentials as well as existing charges. In the examined device, the length of the channel is relatively small compared to the length of the contacts. Also the distance between gate and substrate is more than 8 times the distance between source/drain and substrate (see Fig. 4.1).

Drift-diffusion based simulations performed by M. Gruber and M. Buchner [23] showed that, with this special geometry used and without the presence of charges, the substrate potential adopts approximately the mean value of the drain and source potential. Using the same set of parameters, as defined at the beginning of the section in Tab. 4.1, the influence of the anticipated V_{SUBS} is investigated by calculating the transfer characteristics for $V_{SUBS} = \frac{V_S - V_D}{2}$, i.e., $V_{SUBS} = -12.5V$, $-22.5V$ and $-42.5V$ at $V_D = -25V$, $V_D = -45V$ and $V_D = -85V$. This is compared to the characteristics obtained with $V_{SUBS} = 0V$ in Fig. 4.10. As can be seen, there is not only a significant change in the current, but also in the shape of the curves. These changes increase with the absolute value of V_{SUBS} . Moreover, no threshold voltage can be observed. This is due to a second channel, that is formed at the SiO_x -OSC interface. To illustrate that, the potential distribution and the current density distribution are plotted in Fig. 4.11. In the plot of the potential distribution (Fig. 4.11 (A)) a steep potential drop, i.e., a strong electric field at the SiO_x -P3HT interface (see arrow III) can be observed, even stronger than at the P3HT-PVA interface. This leads to an accumulation of charge carriers at the SiO_x -P3HT interface (see arrow II) and therefore to the formation of a second channel. This second channel can nicely be seen in the plot of the current densities (Fig. 4.11 (B)). Thus, V_{SUBS} can profoundly alter V_{th} independent from a possible presence of NH_3 . It needs to be stressed that the substrate-induced channel can, in principle, totally obscure a possible NH_3 -sensitivity of the PVA-P3HT channel (see arrow I).

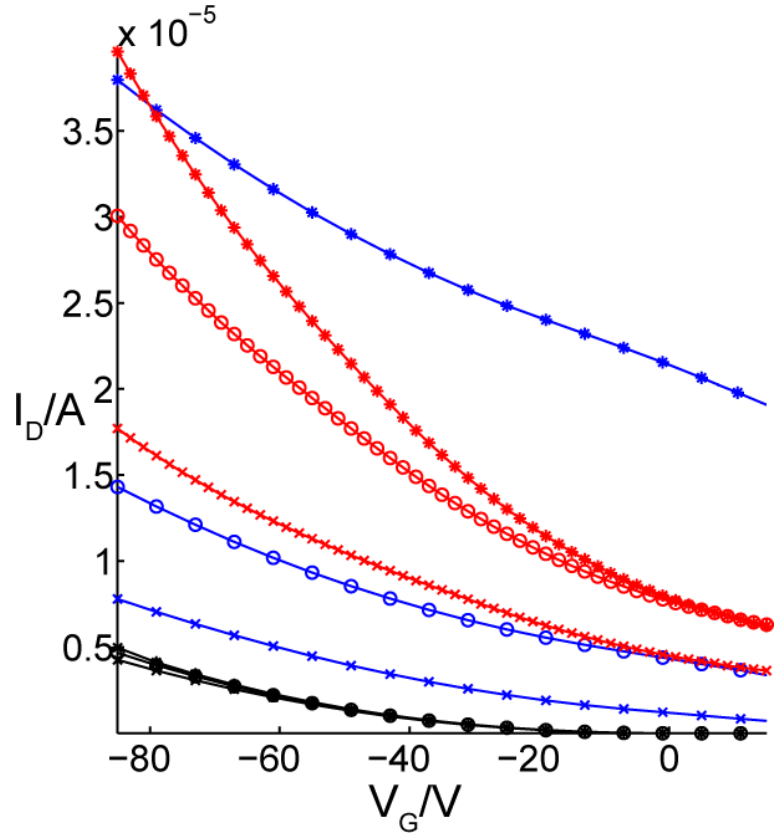


Figure 4.10: Impact of the substrate potential V_{SUBS} on the transfer characteristics (blue) for three different drain potentials: $V_D = -25\text{V}$ (cross), -45V (circle) and -85V (star). The corresponding substrate potentials are $V_{SUBS} = \frac{V_S - V_D}{2} = -12.5\text{V}$, -22.5V and -42.5V . For a better comparison the results for $V_{SUBS} = 0\text{V}$ are plotted (black), as well as the experimental results in exposition to ammonia (red).

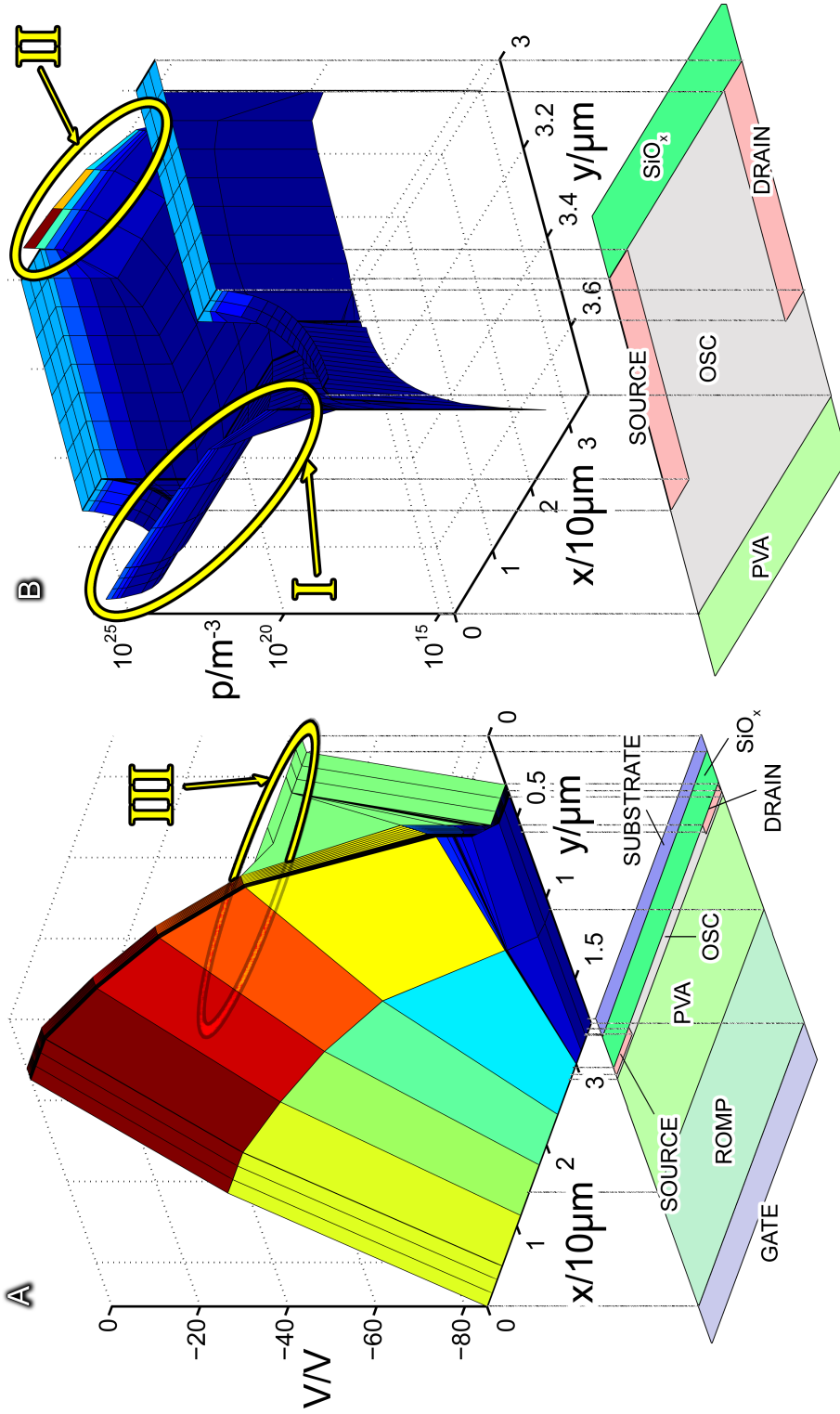


Figure 4.11: (A) Potential distribution and (B) hole density of the device for $V_{SUBS} = \frac{V_D + V_S}{2} = -42, 5V$, $V_D = -85V$, $V_G = -85V$. The substrate potential induces a large electric field at the SiO_x -P3HT interface (arrow III) due to which a second channel is formed (arrow II). Arrow I depicts the gate induced channel.

4.2.2 Comparison of simulation and experiment

Having analyzed the influence of the most important parameters on the transfer characteristic, now these parameters are optimized in order to reproduce the experimental results without ammonia exposure best. This optimal set is then used to verify the three scenarios that were suggested in section 4.1 to explain the ammonia-sensitivity.

4.2.3 Optimization of parameters for a device without the presence of ammonia

The first challenge is to find a set of parameters, which approximate the experimental results best. The main problem, as was established in section 4.2.1, is related to the offset between the individual curves in the simulation compared to the experiment. The simulated curves are much closer together; the influence of the substrate potential was shown to be dominant. Thus, a reasonable spacing could be only generated by assuming 3 different substrate potentials for the three different drain potentials. The parameters that agree best with the experiment, i.e., within 1% are shown in Tab. 4.2. The resulting characteristics in comparison to the experimental results are shown in Fig. 4.12.

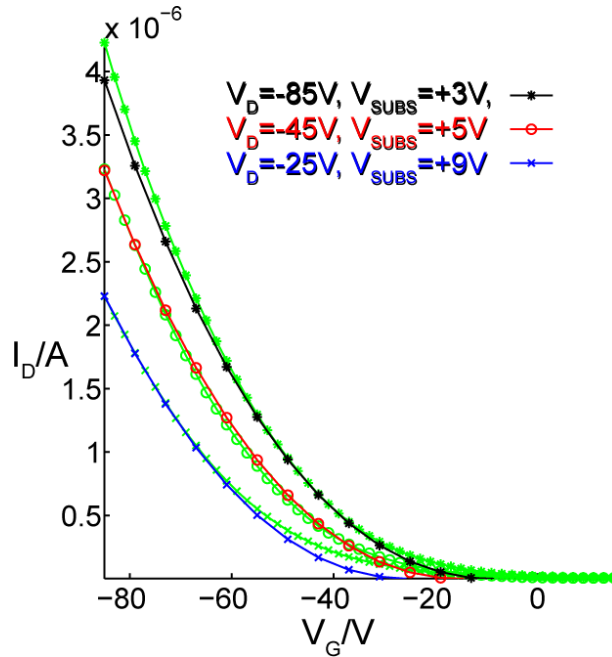


Figure 4.12: Simulated transfer characteristics with optimized parameters (Tab. 4.2) compared to the experimental ones without exposure to ammonia (green)

Table 4.2: Set of parameters used for reproducing the experimental results

μ_0	0.4×10^{-6}	$\frac{m^2}{Vs}$
ϵ_{SiO_x}	4.5	
ϵ_{OSC}	3.2	
ϵ_{PVA}	8.4	
$\epsilon_{ROM-polymer}$	6	
T	298.15	K
N_{HOMO}	2×10^{27}	$\frac{1}{m^3}$
Δ_h	0.1	eV
V_{SUBS}	3	V for $V_D = -85V$
V_{SUBS}	5	V for $V_D = -45V$
V_{SUBS}	9	V for $V_D = -25V$

4.2.4 Simulation of the device exposed to ammonia

As mentioned in subsection 4.1, there are three different possible scenarios to explain the effect seen in the experiment. With the optimized set of parameters found in 4.2.3, these three assumptions are now tested.

Ammonia induced change of the dielectric constant of the ROM-polymer: The first effect considered is the experimentally established change in the dielectric constant of the ROM-polymer ($\epsilon_{ROM-polymer}$) from 6.0 to 6.5 [2]. The results are shown in Fig. 4.13. As easily can be seen, the effect solely resulting from the change in the dielectric constant is by far too small to explain the effects seen in the experimental transfer characteristics. However, this change must be taken into account when testing the other two remaining assumptions.

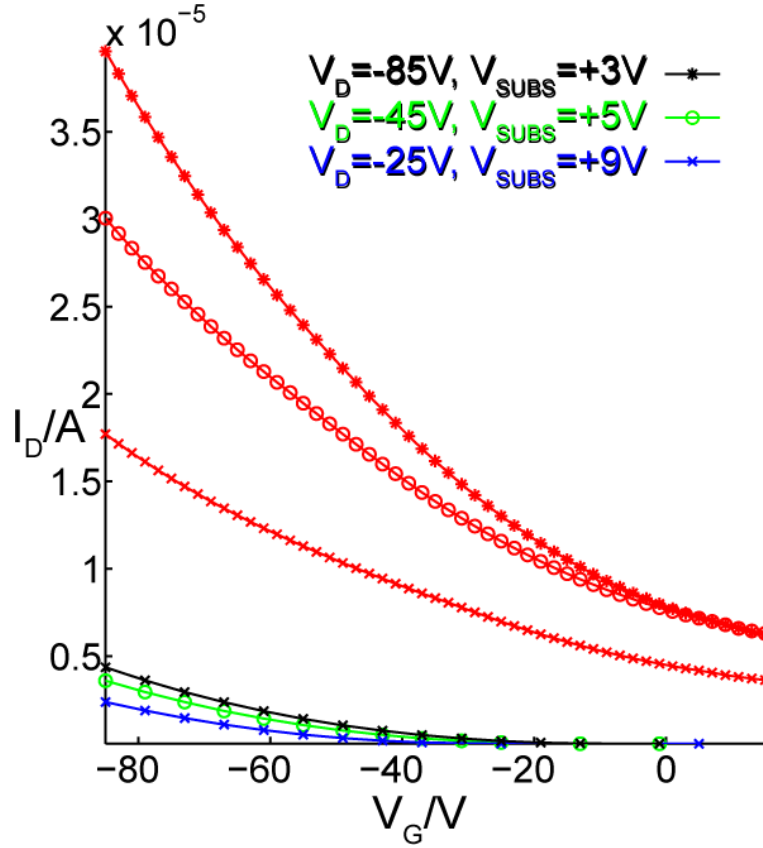


Figure 4.13: Simulation of the influence of a changed dielectric constant on a transfer characteristic in comparison to the experimental results (red).

Ammonia induced space charge layer in the ROM-polymer: The second assumption was a space charge caused by immobile O^- -groups in the ROM-polymer. This is taken into account by a constant negative charge density. Assuming that every polymer repeating unit contains exactly one OH-group, the given density of the ROM-polymer yields a maximum space charge density $\sigma_1 = 7.52 \times 10^{21} \frac{1}{m^3}$ [24], which is incorporated in the model via Eq. (2.7). The characteristics obtained for the consideration of σ , located in the ROM-polymer-layer, are shown in Fig. 4.14. It can be clearly seen that the influence of the immobile charge carrier is not sufficient to explain the large difference between the pristine device and the device exposed to ammonia. Nevertheless, a small increase in the current occurs. While σ_1 might contribute to the experimentally observed effect, it cannot be responsible for the observed effect.

Ammonia induced surface charge layer at the PVA-P3HT interface: The third scenario comprised a layer of negatively charged O^- -groups at the PVA-P3HT inter-

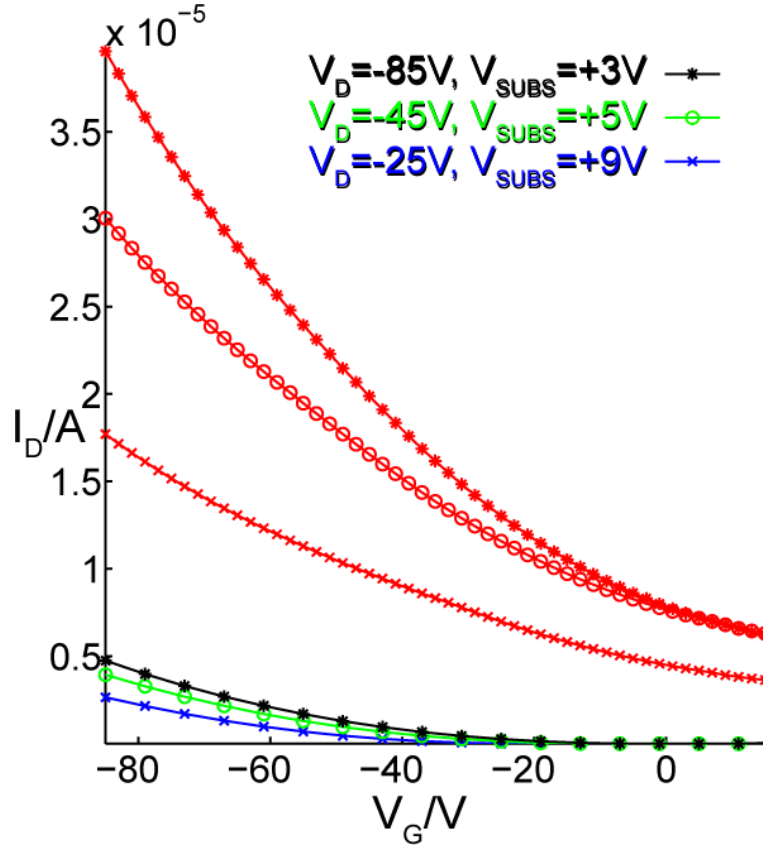


Figure 4.14: Simulation of the influence of the maximum of immobile space charges in the ROM-polymer in comparison to the experimental results (red).

face. Created in the ROM-polymer, the negative charges migrate through the device, and, eventually, accumulate at the interface to the OSC (see subsection 2.3). This is incorporated in the simulation by a surface charge layer with a density σ_2 at the PVA-P3HT interface. In contrast to the immobile-ion model mentioned before, the maximum charges amount to the sum of the OH-groups in the polymer and in the PVA layer. By assuming a surface charge density of $\sigma_2 = 4.5 \times 10^{15} \frac{1}{m^2}$, the simulation reproduces (a) the required increase in current and (b) the absence of a threshold voltage in the interval $-85V < V_G < 15V$. As shown in Fig. 4.15, the simulated results agree well with the measured characteristics, within a maximal error of ca. 10%. A slightly different slope for $V_D = -25V$ and $V_D = -85V$ is observed. This underestimation of the slope originates from the neglect of charge trapping effects in the model presented in this thesis.

In conclusion, the effect observed in the experiment can be reproduced qualitatively and quantitatively by negative mobile charges. Immobile charges and the experimentally

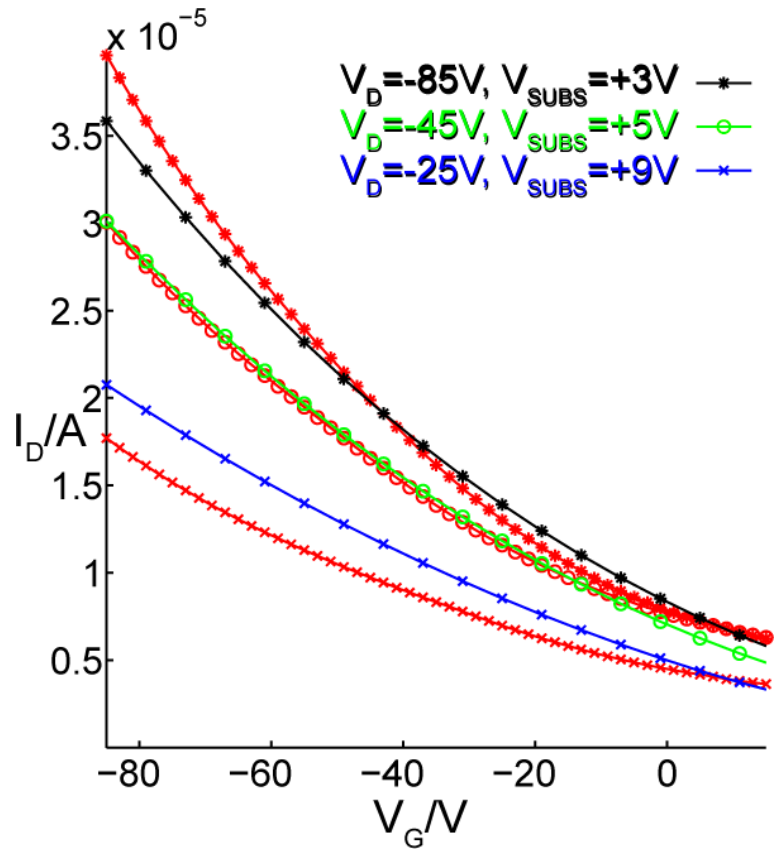


Figure 4.15: Simulation of the influence of a surface charge density at the P3HT-PVA interface compared to the experimental results in presence of ammonia (red).

observed change in the dielectric constant can additionally contribute to the current enhancement.

5 Conclusion

The main task of this thesis was to develop a program capable of simulating the transfer-characteristics under consideration of the charge transport, potential and charge carrier density of a sensory dual-gate OFET, built by Andreas Klug et al. [2]. Experiments showed that this device was highly sensitive to ammonia owing to a ROM-polymer with an Eosin-Y group used as isolating material. In the presence of ammonia the current increased by more than 800%. Additionally no threshold voltage could be observed anymore. Three different scenarios were proposed to explain this effect: a change in the dielectric constant of the ROM-polymer, the formation of a constant negative space charge density in the ROM-polymer due to immobile ions, and the formation of a negatively charged surface charge layer at the PVA-OSC interface. The challenge posed in this thesis was to cope with the high aspect ratio large extensions of the device itself and to incorporate a model able to simulate the behavior upon exposure to ammonia.

In order to simulate this device, a two-dimensional drift-diffusion model was used, resulting in a system of equations (containing the Poisson equation, current density equations and the continuity equation and a density dependent mobility model), which was solved self-consistently on a non-regular two-dimensional grid. Therefore, all these equations had to be transferred in numerical stable expressions and then solved iteratively.

With the help of the model, parameter studies were made to gain insight into the influence of transport-specific parameters on the transfer characteristics. The considered parameters are (a) the dielectric constant of the isolating ROM-polymer, (b) the mobility, (c) the injection barrier between contact and OSC, and (d) the substrate potential.

Based on the insights gained in the parameter study, a certain set of parameters is chosen in order to reproduce the measured data for the OFET operating without ammonia. Then, by fixing these parameters, the three proposed scenarios were tested. Two of them, the change in the dielectric constant of the polymer and the presence of a space charge layer in the polymer, were excluded as dominant causes for the measured effect. On the other hand, a negatively charged surface charge layer at the PVA-OSC interface, arising from O^- -groups that are formed in a chemical reaction with the ammonia in the

5 Conclusion

ROM-polymer and subsequently migrate through the PVA, was able to reproduce the experimentally observed effect with a maximum error of less than 10%.

6 Acknowledgments

I would like to acknowledge and express my gratitude to my advisors Ao. Univ.-Prof. DI Dr. Ferdinand Schürerer and Dipl.-Phys. Dr.rer.nat. Karin Zojer. Without their patience, supervision, advice and support this thesis would never have been completed. Additionally, I want to mention the whole group of Ao. Prof. F. Schürerer, especially Stefan, Manni and Benji. Without them this thesis would never have been finished.

Furthermore, I would like to thank the Christian Doppler Laboratory "Advanced Functional Materials", in particular Ao.Univ.-Prof. Dipl.-Ing. Dr.techn. Emil List, for their financial support.

Last, but not least, I want to thank my family and my friends.

Bibliography

- [1] J. J. Miasik, A. Hooper, B. C. Tofield, "Conducting polymer gas sensors", *Journal of the Chemical Society, Faraday Transactions 1*, 82:1117-1126, 1986.
- [2] A. Klug, "Organic Field-Effect Transistors - Process Development, Stability Issues and Sensor Applications", PhD Thesis, TU-Graz, 2010.
- [3] P. Pacher, A. Lex, V. Proschek, H. Etschmaier, E. Tchernychova, M. Sezem, U. Scherf, W. Grogger, G. Trimmel, C. Slugovc, E. Zojer, "Chemical control of local doping in organic thin-film transistors: From depletion to enhancement", *Advanced Materials*, 20:3142-3148, 2008.
- [4] M. Sandholzer, G. Fritz-Popovski, C. Slugovc, "Synthesis and self assembly of Eosin functionalized amphiphilic block-random copolymers prepared by ring opening metathesis polymerization", *Journal of Polymer Science: Part A: Polymer Chemistry*, 46:401-413, 2007.
- [5] A. Assadi, G. Gustafsson, M. Willander, C. Svensson, O. Inganäs, "Determination of field-effect mobility of poly(3-hexylthiophene) upon exposure to NH₃ gas", *Synthetic Metals*, 37:123-130, 1990.
- [6] M. Schwoerer and H. C. Wolf, "Organic Molecular Solids", Wiley-VCH Verlag, Weinheim, 2007.
- [7] A. Assadi, C. Svensson, M. Willander, and O. Inganäs, "Field-effect mobility of poly(3-hexylthiophene)", *Applied Physics Letters*, 53:195:197, 1988.
- [8] H. Bässler, "Charge transport in disordered organic photo conductors", *Physica Status Solidi B*, 175:15-56, 1993.
- [9] C. Im, "Optoelektronische Eigenschaften von π -konjugierten Polymeren", PhD Thesis, Philipps - Universität Marburg, 2002.

Bibliography

- [10] M. Vissenberg and M. Matters. "Theory of field-effect mobility in amorphous organic transistors", *Physical Review B*, 57:12964-12967, 1998.
- [11] W. Pasveer, J. Cottaar, C. Tanase, R. Coehoorn, P. Bobbert, P. Blom, D.M. de Leeuw, and M. Michels. "Unified description of charge-carrier mobilities in disordered semiconducting polymers", *Physical Review Letters*, 94:1-4, 2005.
- [12] R. Coehoorn, W. Pasveer, P. Bobbert, and M. Michels, "Charge carrier concentration dependence of the hopping mobility in organic materials with Gaussian disorder", *Physical Review B*, 72:1-20, 2005.
- [13] A. Miller and E. Abrahams, "Impurity conduction at low concentrations", *Physical Review*, 120: 745-755, 1960.
- [14] S.M. Sze and K. N. Kwok, "Physics of Semiconductor Devices", Wiley Interscience, 3rd edition, 2007.
- [15] F. Torricelli, Zs. M. Kovacs-Vajna, L. Colalongo, "The role of the density of states on the hole mobility of disordered organic semiconductors", *Organic Electronics*, 10:1037-1040, 2009.
- [16] C. M. Snowden, "Introduction to semiconductor device modeling", World Scientific, Singapore, 1986.
- [17] A. Khaliq, F. L. Xue, K. Varahramyan, "Numerical simulation of spin coated P3HT organic thin film transistors with field dependent mobility and distributed contact resistance", *Microelectronic Engineering* 86:2312-2315, 2009.
- [18] S. Possanner, "Drift-diffusion simulations of charge transport in organic field-effect transistors", Diploma Thesis, TU-Graz, 2008.
- [19] M. Scharnberg, V. Zaporozhtchenko, R. Adelung, F. Faupel, C. Pannemann, T. Diekmann, U. Hilleringmann, "Tuning the threshold voltage of organic field-effect transistors by an electret encapsulating layer", *Applied Physics Letters*, 90:2426926, 2007
- [20] T. Cui, G. Liang , "Dual-gate pentacene organic field-effect transistors based on a nanoassembled SiO₂ nanoparticle thin film as the gate dielectric layer", *Applied Physics Letters*. 86:1861126, 2005.
- [21] B. Stickler, private communication, 2010.

Bibliography

- [22] M. J. Panzer, C. D. Frisbie, "Superconductivity: Interfaces heat up", *Advanced Materials*, 20:3177-3180, 2008.
- [23] M. Gruber, M. Buchner, private communication, 2010.
- [24] C. Slugovc, private communication, 2010.